



PII S0016-7037(01)00704-9

Coupled heat and silica transport associated with dike intrusion into sedimentary rock: Effects on isotherm location and permeability evolution

BARBARA L. DUTROW,^{1,*} BRYAN J. TRAVIS,² CARL W. GABLE,² and DARRELL J. HENRY¹¹ Department of Geology and Geophysics, Louisiana State University, Baton Rouge, LA 70803, USA² Geoanalysis Group, Los Alamos National Lab, Los Alamos, NM 87545, USA

(Received November 6, 2000; accepted in revised form May 24, 2001)

Abstract—An 11-meter-wide alkalic monchiquite dike recovered from the subsurface of Louisiana has produced a metasomatic aureole in the adjacent interbedded carbonate mudstones and siltstones. The asymmetric contact aureole, which extends nearly 6 m above and 4 m below the intrusion, contains the metamorphic minerals, diopside, pectolite, fluor-apophyllite, fluorite, and garnet. A series of coupled heat and mass transport calculations was undertaken to provide thermal constraints for the aureole, in the absence of robust geothermometric assemblages, and insights into accompanying mass transport associated with the sedimentary rock–dike system.

Calculations were completed for systems with homogeneous, anisotropic, and layered permeability, κ . Transport, dissolution, and precipitation of silica were also incorporated into calculations. All systems modeled indicate that the thermal pulse waned in ~ 3 yr with a return to background temperatures in ~ 10 yr. Heat and fluid transport produce maximum temperature isotherms that are distinctly different in spatial extent and lateral variability for each numerical system. The homogeneous κ case produced isotherms that pinch and swell vertically above the dike and have large lateral variations, in contrast to the anisotropic κ case that produced a single large plume above the dike. The layered system κ case produced the most spatially extensive thermal aureole, unlike that recorded in the rocks.

Addition of dissolved silica to the flow system significantly impacts the calculated transport of heat and fluid, primarily due to density changes that affect upwelling dynamics. Although precipitation and dissolution of SiO_2 can affect flow through the feedback to permeability, κ changes were found to be minor for these system conditions. Where κ decreased, flow was refocused into higher κ zones, thus mitigating the κ differences over time. This negative feedback tends to defocus flow and provides a mechanism for lateral migration of plumes. Coupled heat and silica transport produces a complex isotherm geometry surrounding the intrusion due to formation of upwelling and downwelling plumes and lateral translation of plumes, leading to variability in the isotherm pattern that does not reflect the inherent heterogeneity of the initial material properties. Initial heterogeneities in κ are not a prerequisite for the development of a complicated flow and transport pattern. In addition, if isotherms reflect isograds, these calculations demonstrate that isograds may not form uniform structures with isograd boundaries characterized by their distance from the heat source. Copyright © 2001 Elsevier Science Ltd

1. INTRODUCTION

The intrusion of igneous rocks into organic-rich sedimentary rocks has been implicated in the maturation of oil and gas in regions where simple burial in a sedimentary basin is insufficient to attain temperatures required for thermal maturation of the attendant organic material (120–160°C; e.g., Sassen and Moore, 1988; Blatt, 1992; Glikson et al., 2000). In concert with the transfer of heat associated with the cooling intrusion, chemically distinct fluids may infiltrate the host rocks to produce a metasomatic aureole proximal to the intrusive body (Raymond and Murchison, 1988). One example of this phenomenon is in the large Monroe Gas Field (MGF) located in the Monroe Uplift, northeastern Louisiana (Fig. 1). The MGF lies in the window of “oil condensates” and is north of the presumed zone for hydrocarbon thermal maturity (Echols et al., 1994). On the basis of isotopically heavy $\delta^{13}\text{C}$ of methane (-43.3% PDB, Peedee Belemnite; Zimmerman and Sassen, 1993), isotopically light (-27.5% PDB) $\delta^{13}\text{C}$ of carbon dioxide (ibid, Sassen and

Moore, 1988), and the location of the field, organic maturation is consistent with associated igneous activity.

Evidence of igneous rocks in the subsurface is identifiable from gravity studies (Lyons, 1957) or from direct observation in conventional drill cores extracted from the subsurface. The MGF coincides with the Monroe uplift, a major structural feature in the northern Gulf Coast (Fig. 1). Like the Jackson Dome, Mississippi, and the Sabine Uplift which borders Texas and Louisiana, the Monroe Uplift is associated with igneous activity as indicated by the presence of igneous rocks extracted from numerous deep wells (Kidwell, 1949, 1951; Moody, 1949). Most intrusions encountered are Mesozoic in age, alkalic in composition, and classified roughly as lamprophyres (Kidwell, 1951; Byerly, 1991).

One such dike is present in a drill core extracted from the Monroe Uplift, subsurface Louisiana (Fig. 2). To ascertain the magnitude of the thermal and chemical influence of this dike on the surrounding hydrocarbon-rich sediments and the likelihood of such intrusions providing the heat for thermal maturation, a series of heat and mass transport calculations was completed for this geologic system as constrained by previous petrologic, mineral chemical, geochemical, and analytical studies (Heydari et al., 1997; Christensen, 1997; Dutrow et al., 1997).

* Author to whom correspondence should be addressed (dutrow@geol.lsu.edu).

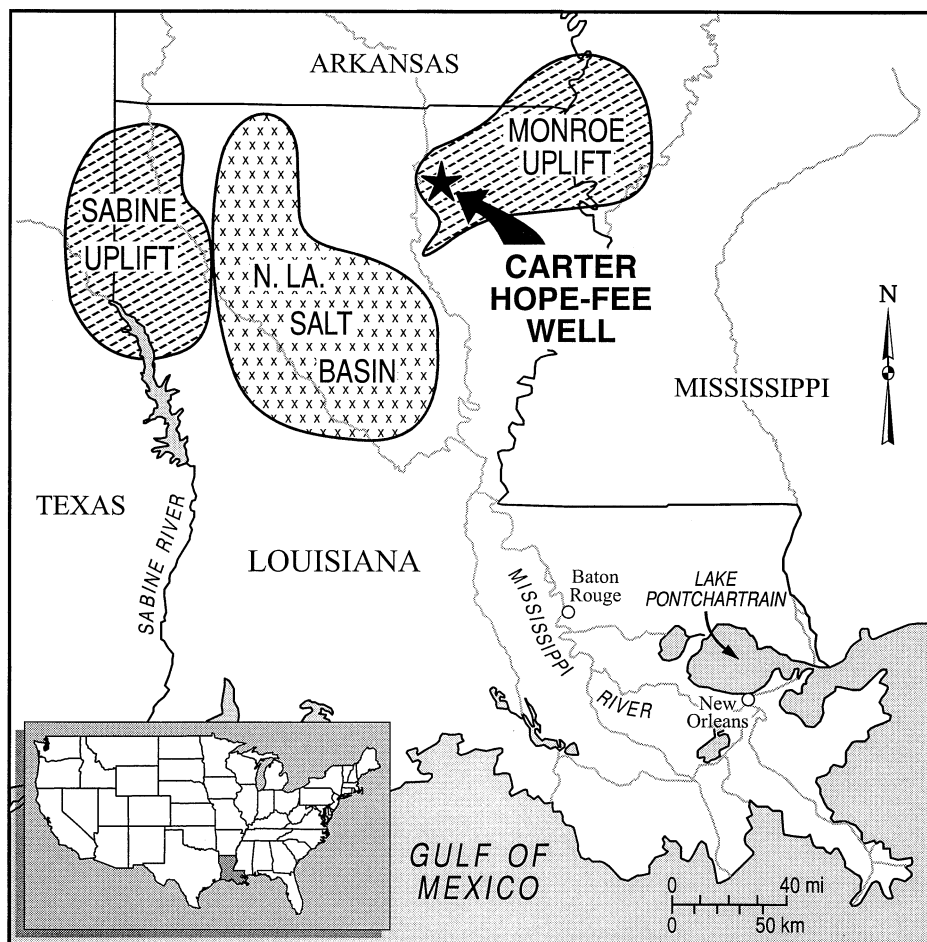


Fig. 1. Location of the drill core extracted from the Carter #1 Hope-Fee Well in the Monroe Gas Field, LA, with associated structural features of the region.

2. GEOLOGIC SETTING AND BACKGROUND

The drill core is from the Carter #1 Hope-Fee Well, northeast Louisiana (Fig. 1). The core includes an 11-m-wide dike penetrating a section of thinly bedded laminated carbonate mudstones and organic-rich siltstones of the upper Jurassic Smackover Formation, a hydrocarbon-rich source rock, at a depth of 2.1 km (Fig. 2; Heydari et al., 1997).

2.1. Dike Description

The dike is a porphyritic lamprophyric intrusion similar in mineralogy and major element chemistry to other Late Cretaceous igneous rocks of the region (Byerly, 1991; Heydari et al., 1997). The characteristic phenocrysts are predominantly complexly zoned titanite with lesser amounts of titanite, apatite, biotite, titanomagnetite, and partially resorbed amphiboles. The phenocrysts are set in a groundmass primarily comprised of analcime. At the lower margin of the dike, the groundmass is a uniform pale brown devitrified glass. Major and trace element compositions are generally similar in the dike interior and margin (based on the three samples analyzed; Heydari et al., 1997). The dike is nepheline normative and, based on the chemistry and mineralogy, is classified as a monchiquite (ibid.).

Geologic reconstructions of the region suggest that the dike was intruded at approximately the same depth as it currently occurs, 2.1 km, and constrain the age of the igneous activity to be late Cretaceous to earliest Paleocene (Heydari et al., 1997). The low pressure of crystallization mandated by the 2.1 km intrusion depth implies that the analcime in the dike is probably secondary. Primary igneous analcime (+ melt) is considered to be stable only at higher pressures, 5–13 kbar, at about 600°C (Roux and Hamilton, 1976).

2.2. Host Rock Description

The Smackover sediments unaffected by the intrusion range in composition from pure calcitic mudstones with minor organic material to organic-rich siltstones. Although modal amounts of the minerals vary considerably, the dominant mineral assemblage in these sediments is fine-grained calcite + detrital quartz + framboidal pyrite + organic material. Minor amounts of dolomite, anhydrite, and clay minerals have also been observed locally (Heydari et al., 1997). However, dolomite has not been observed in the aureole rocks. Trace detrital grains include muscovite, tourmaline, rutile, plagioclase, zircon, apatite, titanite, and ilmenite (Dutrow et al., 1997).

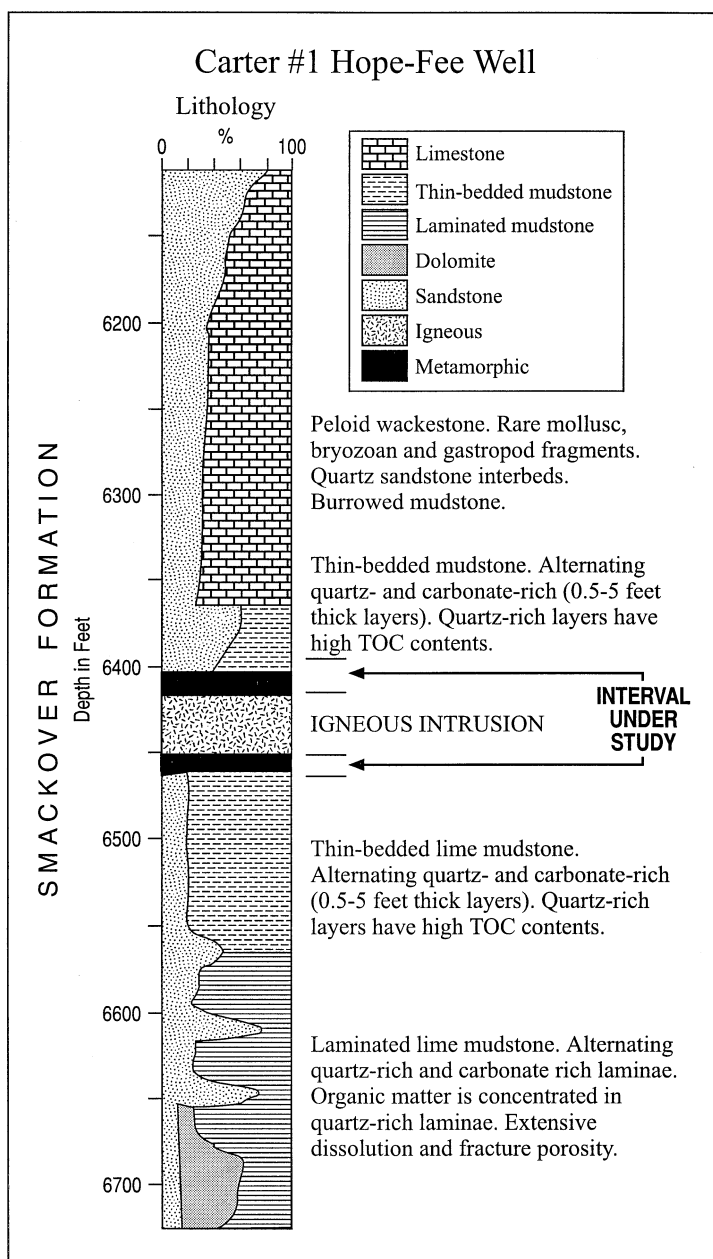


Fig. 2. Stratigraphic section of the drill core interval containing the dike under study (after Heydari et al., 1997).

2.3. Contact Aureole

The metamorphic aureole, defined in part by C and O isotopic alteration, extends into the host sediments to ~6 m above and ~4 m below the dike (Heydari et al., 1997). The calcite in sedimentary rocks distant from the dike has a $\delta^{18}O$ of -4% PDB, which decreases irregularly to -15% PDB, at the intrusive contact (all values are $\pm 0.2\%$ precision). The $\delta^{13}C$ of the calcite in the unaltered host rocks is near $+4\%$ PDB and decreases to -7% PDB proximal to the dike. In addition, the total organic content of the background sedimentary rocks averages roughly 0.7% but decreases systematically to 0.1% near the contact. Heydari et al. (1997) note that this style of

covariation of $\delta^{18}O$ and $\delta^{13}C$ in a contact aureole is consistent with thermal effects and fluid infiltration associated with an intrusion. Based on the calcite $\delta^{18}O$ adjacent to the dike, Heydari et al. (1997) estimate that the contact aureole attained temperatures in the range 340–440°C, and that temperature influences reflected in isotopic variations progressively decrease to background levels.

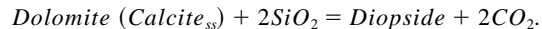
Adjacent to the dike, clear mineralogical changes occur in the sediments that reflect development of a contact metamorphic aureole. The new metamorphic/metamorphic minerals include diopside, K-feldspar, albite, pectolite, fluor-apophyllite, grossular garnet, fluorite, and pyrrhotite (Christensen, 1997; Dutrow et al., 1997; Table 1). Most of these minerals are

Table 1. Formula for metamorphic minerals observed in the contact aureole.

Calcite	$CaCO_3$
Diopside	$CaMgSi_2O_6$
K-feldspar	$KAlSi_3O_8$
Pectolite	$NaCa_2Si_3O_8(OH)$
Fluorite	CaF_2
Apophyllite	$KCa_4Si_8O_{20}F \cdot 8H_2O$
Grossular	$Ca_3(Al, Fe^{3+})_2Si_3O_{11.85}(F, OH)_{0.15}$
Analcime	$NaAlSi_3O_6 \cdot H_2O$
Sodalite	$Na_8Al_6Si_6O_{24}Cl_2$

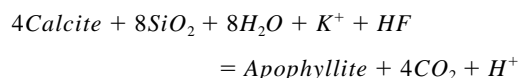
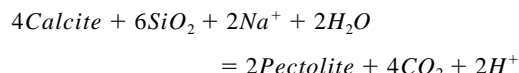
enriched in alkali and alkaline earth elements as well as fluorine relative to the initial sedimentary mineral assemblage. Equally as notable is the progressive disappearance of quartz in metasediments as the dike contact is approached. In the heterogeneous thinly bedded protoliths most mineralogical changes occur in siltstone-rich areas, but recrystallization is also observable in the carbonate mudstones.

As the intrusion is approached, textural and mineralogical changes take place in the fine-grained metasedimentary rocks. (1) Veins of recrystallized calcite are the first notable metamorphic feature developed at roughly 4 m above and 2.4 m below the dike. (2) At roughly 2.5 m above and 1.8 m below the dike, trace amounts of near end-member diopside, $(Ca_{0.98}Na_{0.01})(Mg_{0.97}Fe_{0.05})(Al_{0.03}Si_{1.97})O_6$, form as anhedral grains near calcite and quartz, likely as a consequence of the dolomite component in calcite reacting with quartz to form diopside via the reaction:



At these distances fine-grained albite ($Ab_{\sim 99}$) is rimmed by K-feldspar (Or_{96}) in the siltstone layers. The coarser organic material has been converted to graphite. These mineral relations persist up to the intrusive contact.

(3) Near end-member pectolite, $NaCa_2Si_3O_8(OH)$, appears at 1.5 m above and 0.6 m below the intrusion, and locally constitutes a major mineral constituent ($\geq 50\%$) up to the contact. Pectolite commonly pseudomorphs detrital quartz grains, but also develops as ≥ 1 -mm pods with rims of coarser calcite and fluorite cubes. It is commonly intergrown with euhedral recrystallized pyrite cubes and associated with poikiloblastic fluor-apophyllite, $KCa_4[Si_8O_{20}](F_{.7}OH_{.3}) \cdot 8H_2O$. The reactions that likely account for the development of these minerals are:



(4) Small ($\sim 100 \mu m$), euhedral anisotropic Ca-rich garnet crystals develop in a single unit 0.3 m above the contact and are associated with fluor-apophyllite, pectolite, and pyrrhotite. Core compositions are near end-member grossular, $(Ca_{2.97}Mg_{0.02})(Al_{1.80}Fe_{0.14}Ti_{0.05})(Si_{2.97}Fe_{0.05}^{3+})O_{12}$ with rims that are enriched in F, $(Ca_{2.97}Mg_{0.21})(Al_{1.56}Fe_{0.24}^{3+}Ti_{0.05})(Si_{2.84}Fe_{0.05}^{3+}(F/4)_{0.07}(OH/4)_{0.05})O_{11.84}$.

(5) At the contact with the dike, calcite-rich layers contain end-member analcime ($NaAlSi_3O_6 \cdot H_2O$), fluorite, and zoned sodalite. Sodalite cores are near end-member composition ($Na_8Al_6Si_6O_{24}Cl_2$) but rims have up to 0.27 Ca substituting for Na (Dutrow et al., 1997).

The composition of these minerals and the probable mineral-forming reactions necessitate that metasomatic alteration was an important process that accompanied the thermal overprint of the sedimentary rocks near the dike. The early formation of sodic minerals, e.g., albite, pectolite, and analcime, in a Na-poor environment implies that Na was introduced initially from the fluid. The crystallization of poikiloblastic fluor-apophyllite and K-feldspar rims on albite implies a later influx of fluids with increasing α_{K^+} and probably decreasing α_{H^+} (e.g., Bowers et al., 1984). In addition, the occurrence of fluorite, fluorite cores to veins, fluor-apophyllite, and F-bearing rims on the garnets suggests the participation of a late F-enriched fluid. The likely pectolite- and apophyllite-forming reactions not only require the addition of alkali ions in solution, but also the consumption of SiO_2 from preexisting quartz or from silica introduced by the fluid phase. These observations suggest that advective transport of chemical components accompanied the transport of heat during emplacement and cooling of the dike.

Phase equilibria calculations using the pressure of emplacement for the dike, the compositions of the minerals in the aureole, and the database of Berman (1988, 1991) can place some constraints on the temperature and fluid composition in the aureole. The presence of graphitized organic material and Fe^{3+} in the garnet suggests conditions more oxidizing than QFM but lower than NNO. Therefore, the dominant C-bearing fluid species at these P-T conditions was CO_2 rather than CH_4 but the fluid was nearly pure H_2O (Ohmoto and Kerrick, 1977; Spear, 1993, p. 652). The presence of the assemblage diopside + calcite + quartz rather than tremolite in the aureole mandates a temperature of at least 350°C, but probably no more than 400°C for a H_2O -rich fluid [$X(H_2O) \geq 0.95$]. These conditions were attained as far as 2.5 m from the dike margin (diopside zone; Christensen, 1997). The presence of calcite + quartz and the absence of wollastonite indicates that the maximum temperature at the contact was no more than 480°C for a H_2O -rich fluid. The presence of grossular garnet 0.3 m from the dike implies a temperature in excess of 420°C at that point. The F-bearing grossular formed at temperatures between 200° and 420°C near the Skaergaard intrusion (Manning and Bird, 1990) is consistent with these temperatures. Although dolomite is not present, the Mg content of calcite (Anovitz and Essene, 1987) can be used to provide a minimum temperature of 320°C for metacarbonates at 2.5 m above the dike.

The thermal conditions nearest the dike are also generally consistent with the calcite $\delta^{18}O$ temperature estimates in the range 340–440°C (Heydari et al., 1997). To provide additional insights into the local thermal history and advective mass transport in the sedimentary rock–dike system, computational experiments of coupled heat and mass transport were undertaken.

3. METHODS

Thermal history of the dike and host sediments was reconstructed (modeled) with a 3D integrated finite difference computer code, MOR3D (see Appendix and Travis et al., 1991 for details). MOR3D

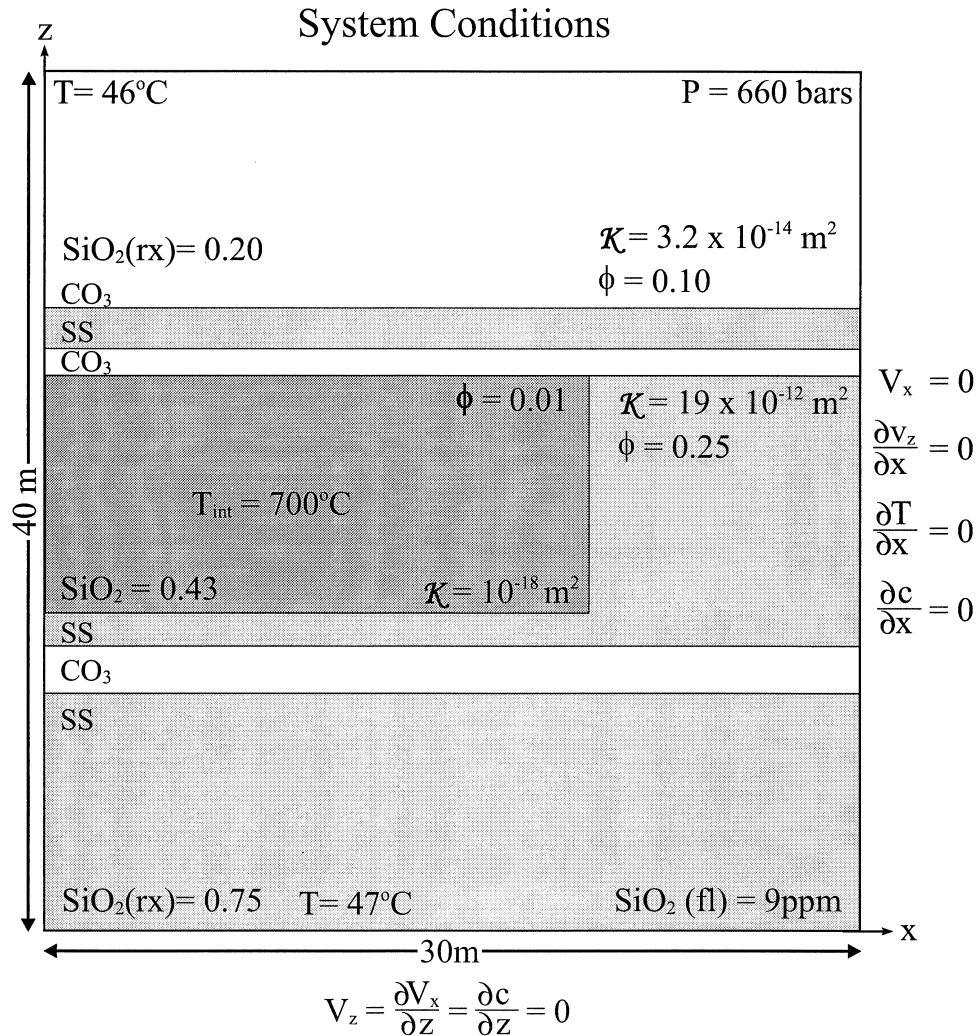


Fig. 3. Initial and boundary conditions for the 2D computational study. Shading differentiates the units used for the layered permeability calculations. Siltstone-rich layers (SS) are in light gray, the carbonate mudstone layers (CO_3) are in white. The darker rectangular area represents the dike. Definitions given in Table 2.

solves a simultaneous set of partial differential equations that describe time-dependent flow through saturated porous media by advection, diffusion, and dispersion. Equations are solved for the conservation of fluid mass, fluid momentum, energy, and species (see Appendix for equations). A full equation-of-state for fluid properties is used for H_2O -rich fluids (Johnson and Norton, 1991). To analyze this system, equations are also incorporated which account for the effects of cooling intrusions by including terms for latent heat of crystallization and for a transient permeability structure of the intrusion. As the intrusion cools and solidifies, it is allowed to fracture and the effective permeability of the dike increases. Transport of SiO_2 was also included in the calculations and changes to permeability, κ , resulting from silica dissolution and precipitation/reaction were incorporated to provide a dynamically changing permeability field (see Appendix, Eqns. A6–A8.). SiO_2 appears to have been mobile in the system because quartz was absent in siltstones adjacent to the dike. In addition, transport of components clearly took place and SiO_2 was used as a proxy for element mobility.

3.1. System Conditions

Because thermal effects on the host rock are localized near the dike margin, calculations were focused on a small area 40 m in height and 30 m in width (Fig. 3). Details of heat and mass transport adjacent to

the dike were estimated using a high-resolution finite difference grid. Most experiments are based on a 2D simplified domain. To capture the detailed lithological variations revealed by the core, a computational mesh with 30×76 (x, z) small, unequal, grid cells surrounding the dike was used. Resolution in z varied from 0.1–1 m. Evenly spaced cells were used for 3D calculations ($50 \times 50 \times 50$; x, y, z). Initial conditions for all numerical systems are: a fluid-saturated porous medium; a static fluid; and permeability, porosity, and silica concentrations uniform within stratigraphic units (Fig. 3). Geologic units overlying the dike are less permeable burrowed mudstones and below the dike, lime mudstones (Heydari et al., 1997). Therefore, boundary conditions for all models were an impermeable top and bottom and sides that are insulating with no fluid flow across the boundary (Fig. 3). The top boundary pressure (P), 660 bars, is lithostatic, but pore fluid pressure within the domain is hydrostatic. The initial temperature at the top boundary of the domain is $46.6^\circ C$ and assumed to vary along a geothermal gradient of $25^\circ C/km$ (Table 2).

Initial conditions for silica concentrations are based on measured values of silica for the dike rock (by X-ray fluorescence [XRF], Heydari et al., 1997), for Smackover fluids (Moldovanyi and Walter, 1992), and for sediments (based on petrographic analyses, Heydari et al., 1997). Modal amounts of quartz limit the total mass of silica available in the system for dissolution. Silica contents of the fluid in the

Table 2. Input parameters and definitions for calculations.

Parameter	Homogeneous κ	Anisotropic κ	Layered κ
Horizontal permeability, $\kappa_{x,y}$ (m^2) host	1.9×10^{-12}	1.9×10^{-12}	3.2×10^{-14} (CO_3) 1.9×10^{-12} (SS)
Vertical permeability, κ_z (m^2) host	1.9×10^{-12}	1.9×10^{-13}	3.2×10^{-14} (CO_3) 1.9×10^{-12} (SS)
Melt permeability, κ_{melt} (m^2)	1.9×10^{-18}	1.9×10^{-18}	1.9×10^{-18}
Fracture permeability, κ_{frt} (m^2)	1.9×10^{-16}	1.9×10^{-16}	1.9×10^{-16}
Dike porosity, ϕ_{dike}	0.01	0.01	0.01
Host rock porosity, ϕ_{hr}	0.25	0.25	0.1 (CO_3) 0.25 (SS)
Intrusion temperature, T_{int} ($^{\circ}C$)	700	700	700
Temperature solidus, T_{solid} ($^{\circ}C$)	650	650	650
Fracture temperature, T_{frt} ($^{\circ}C$)	550	550	550
Thermal diffusivity of saturated porous media ($m^2 s^{-1}$)	1×10^{-6}	1×10^{-6}	1×10^{-6}

CO_3 = carbonate mudstones; SS = siltstones.

dike were assumed to be at equilibrium for the initial pressure and temperature conditions. Equilibrium silica solubility was used, with dissolution and precipitation calculated from quartz solubility (data from SUPCRT92, Johnson et al., 1992; Walther and Helgeson, 1977). While kinetic factors are clearly important in many systems (e.g., Canals and Meunier, 1995; Bolton et al., 1999), general features and effects of the thermal and flow field emerge from calculations for a system in equilibrium and have been used successfully to explore convection in sedimentary basins (e.g., Ludvigsen et al., 1992).

The permeability structure exerts a dominant influence on the flow field, which in turn, impacts energy and mass transport (Norton, 1979). Permeability distributions used include isotropic, homogeneous, and heterogeneous κ structures for the host rocks (Table 2). Heterogeneities in permeability are represented with either a layered permeability structure or anisotropic permeability, or both. For systems preserving the broad-scale stratigraphy, different permeability and porosity values were assigned to the layers of carbonate mudstones (CO_3), $\kappa_x, \kappa_z = 3.2 \times 10^{-14} m^2$, $\phi = 0.1$, and siltstones, $\kappa_x, \kappa_z = 1.9 \times 10^{-12} m^2$, $\phi = 0.25$ (Table 2), in accordance with measured values for the Smackover formation (Clarke, 1966; Garven et al., 1993; Nunn, 1998, personal communication). Anisotropic permeability for a uniform system captured the compacted nature of the sediments, which suggests that flow will occur preferentially parallel to bedding and be inhibited perpendicular to preferred orientation of mineral grains. Consequently, κ_x was set to an order of magnitude larger than κ_z . For comparison, homogeneous, isotropic permeability, which approximates the very fine scale interbedded sediments and which substantially decreases computational time, was also tested as an end-member case (Table 2).

Calculations commence when an 11-m dike (sill) is instantaneously intruded into the sediments. Although the initial melt temperature is uncertain, based on the undersaturated, alkalic nature of the dike, the initial intrusion temperature, T_{int} , is set at 700°C (Carmichael et al., 1974; Wendlandt, 1997, personal communication). Higher initial T_{int} produce higher temperatures in the aureole and larger aureoles (see Dutrow et al., 1997 for calculations with $T_{int} = 875^{\circ}C$). The melt is assumed to be impermeable initially (Table 2). At 100°C below solidification temperature, T_{solid} , it is assumed to fracture (Norton and Knight, 1977), and permeability increases to κ_{frt} (Table 2). These increases occur gradually over time as the intrusion cools to the fracture temperature, with the outer portion of the dike fracturing first followed by the central portion. This permits limited fluid flow through the dike after cooling, in keeping with the late-stage fractures noted at the dike margin. Because the dike had a chilled, glassy margin and because the latent heat for the glass transition is much lower than the latent heat of crystallization (ca. 1%; Navrotsky, 1981), the latent heat term was assumed to be minor and set to zero in all calculations. (For a discussion of the effects of latent heat on the surrounding isograds, see Dutrow et al., 1997). Calculations continued until the average temperature of the system was within 15% of the T prior to dike emplacement.

3.2. Cases

Calculations were completed varying parameters that primarily control the spatial extent of the aureole and the maximum temperatures attained in the thermal aureole. Most calculations were completed for a two-dimensional system; however, selected 3D calculations were done to provide a better interpretation of the 2D models.

At selected times, the evolution of the thermal, SiO_2 fluid concentration, velocity, and pressure fields were examined. Fluid flux is tracked throughout the calculation to provide a time-integrated volumetric flux as a function of position. Calculations record the time and value of maximum temperature, T_{max} , at all locations in the system to provide a map of peak temperatures attained within the aureole. If kinetics were sufficiently rapid, peak temperatures should be recorded in the mineral assemblages and, thus, T_{max} allows for comparison of field data with calculations. Computed results are then compared with the basemap developed from mineral, chemical, and petrologic studies in order to constrain the thermal and metasomatic history related to dike intrusion.

4. RESULTS

For all cases, calculations demonstrate that the thermal pulse was short-lived. Within about 10 yr elevated temperatures decline to near background conditions. In addition, an asymmetric contact aureole developed in host rocks; the size and extent determined by the heat and fluid transport, which is largely controlled by the permeability field. For the systems modeled, differing permeability structures result in distinctly different thermal signatures in the host sediments overlying the dike whereas similar signatures occur beneath the dike. Results of three series of calculations differentiated by the permeability values, isotropic homogeneous, anisotropic homogeneous, and layered (isotropic within layers), are described with respect to the evolution of the thermal and fluid flow fields, silica transport and attendant permeability changes from SiO_2 dissolution and precipitation/reaction, and maximum temperatures attained in the contact aureole.

4.1. Isotropic, Homogeneous Permeability

After instantaneous intrusion of the dike into the cooler country rocks, a buoyant plume develops off the top end of the dike and rises vertically (Fig. 4a,b). Additional plumes form inboard of the dike's lateral extent in response to the formation

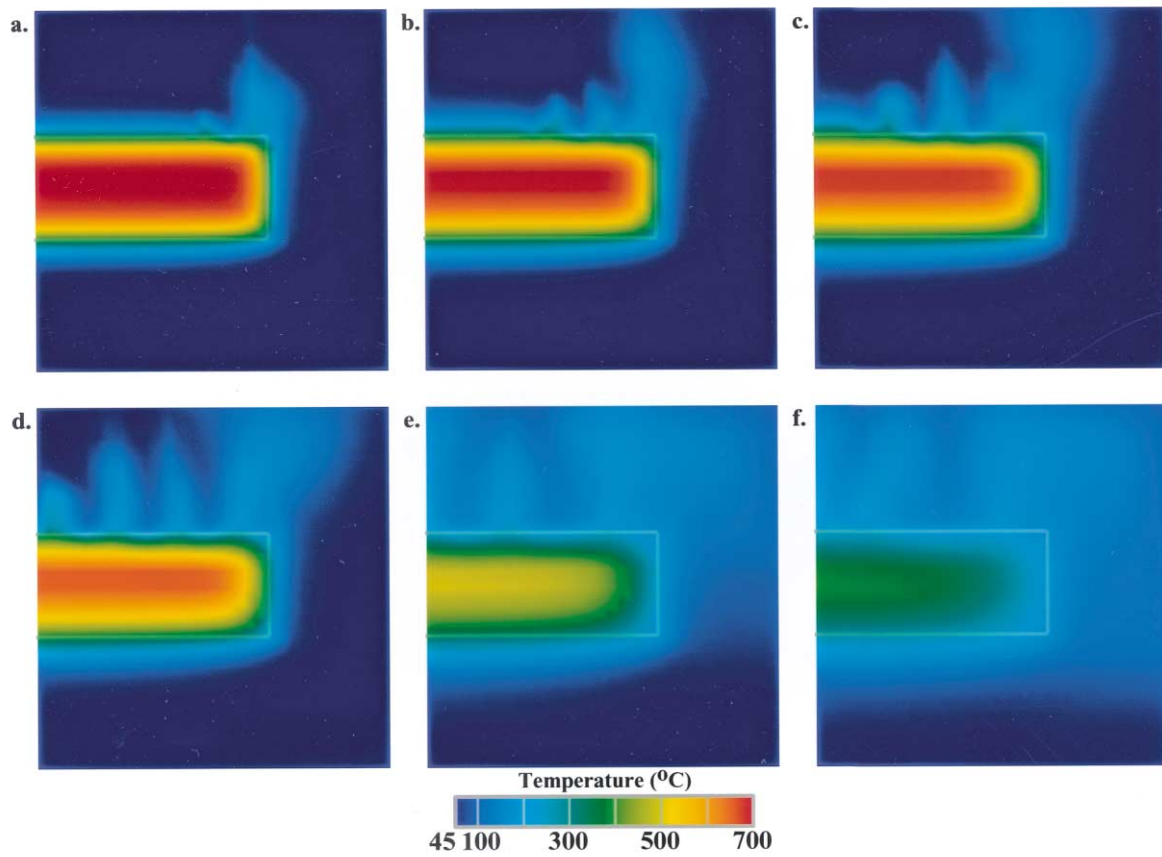


Fig. 4. Evolution of the thermal field for the homogeneous κ , 2D system as a function of time. (a) 0.05 yr, (b) 0.08 yr, (c) 0.1 yr, (d) 0.14 yr, (e) 0.4 yr, (f) 0.8 yr. Gray box outlines the dike.

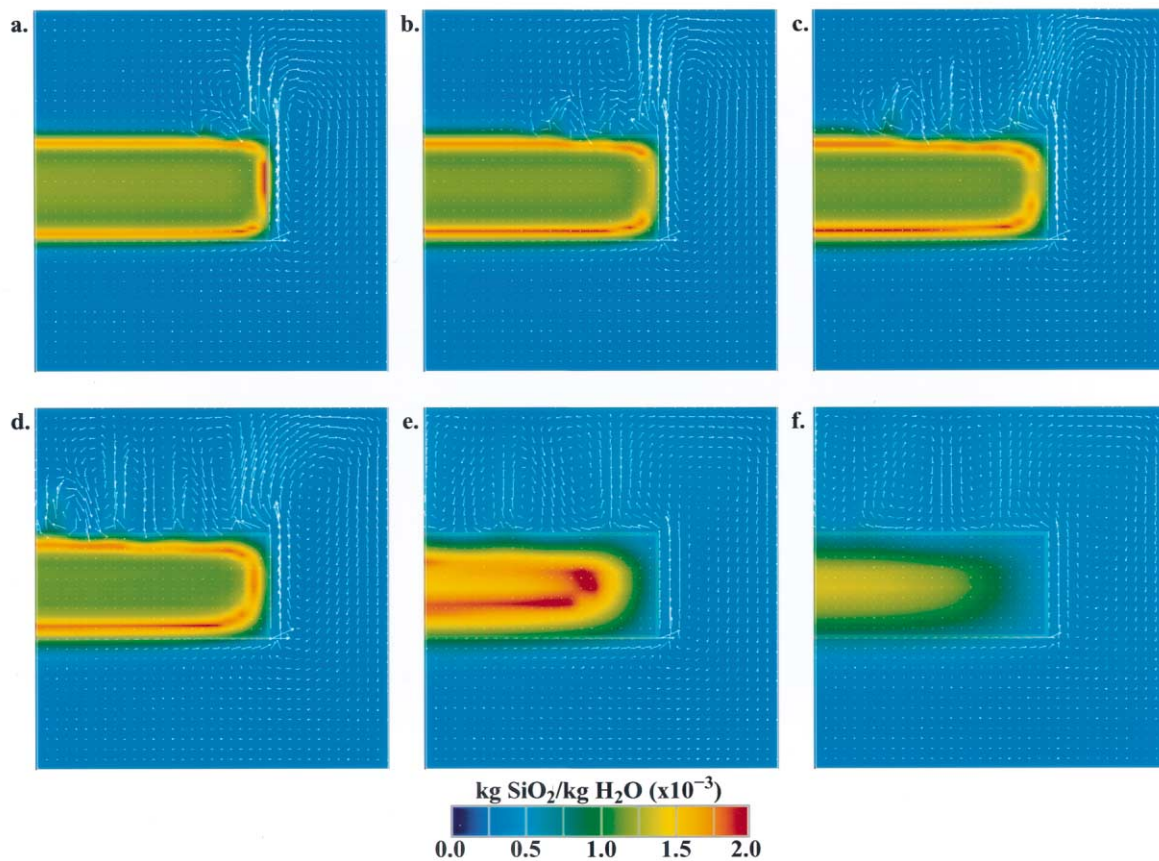


Fig. 5. (a–f) Transport of silica in the fluid for homogeneous κ as a function of time (t given in Fig. 4) with velocity vectors that indicate the direction and magnitude of instantaneous flow. Gray box outlines the location of the dike.

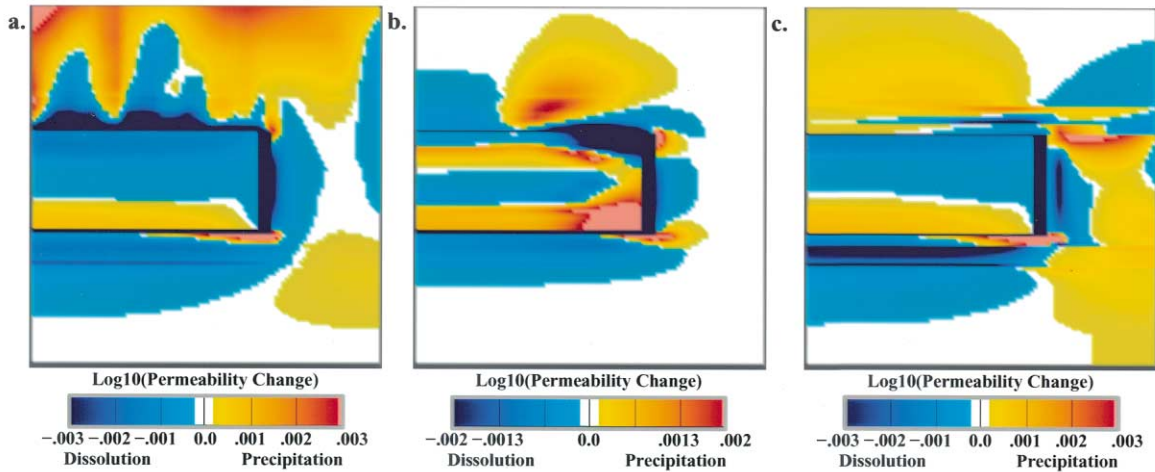


Fig. 6. Time-integrated permeability change (initial-final) resulting from complex feedback of silica transport and reaction for calculations with: (a) homogeneous κ distribution, (b) anisotropic κ distribution, and (c) layered κ distribution. The location of the dike is shown in gray. The coarseness of the color contours is due to the abrupt change in color, in contrast to a smoothly varying color scheme. White = no change and separates areas of dissolution from precipitation. Note the color break at the end of the scale to indicate values out of range.

of an unstable boundary layer of hot fluid above the horizontal dike surface. With continued thermal evolution, a maximum of four distinct plumes develop above the dike in the half space

shown (Fig. 4c,d, a total of eight would develop for this system). The number of plumes that develop is dictated by the size of the system and the roughness of the dike–sediment

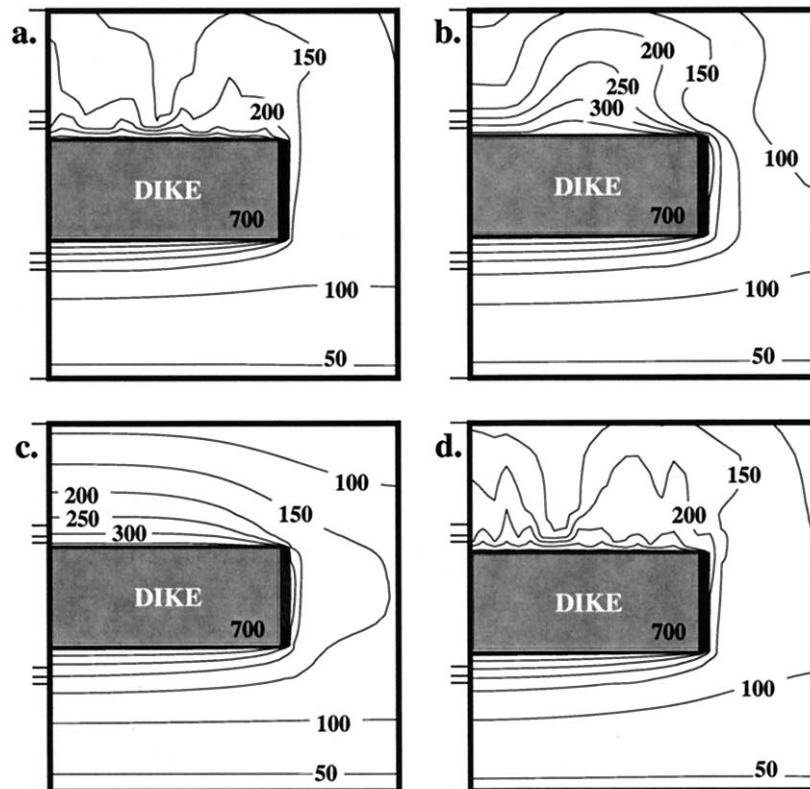


Fig. 7. The maximum temperature T_{max} attained throughout the system, which is independent of time, contoured at 50°C intervals. (a) For the homogeneous κ system, note the distinct upwelling recorded in T_{max} and the laterally variable thermal field; (b) the anisotropic κ system, which produces one large upwelling which thins on either side; (c) the layered κ system, which results in a more laterally uniform aureole and (d) homogeneous κ system without SiO_2 . Dike is shown by the gray box. Lines on left mark mineral zones.

interface, and scales positively with size. The narrow upwellings, separated laterally by adjacent downwellings, are restricted to areas above, and adjacent to, the dike. With continued dissipation of thermal energy, upwellings migrate laterally, coalesce, and become more diffuse as the thermal driving force subsides (Fig. 4e,f). Two upwellings remain centered over the pluton after the initial thermal pulse has passed (e.g., $dT/dt < 0$; Fig. 4e). The plume proximal to the lateral extent of the dike continues its vertical ascent, but is driven primarily by fluid that escapes from the horizontal layer below the intrusion, around the less permeable dike (Fig. 4e). Below the intrusion, the dike cools primarily by horizontal advective heat transfer with diffusion to produce a narrow zone of elevated temperatures. By 1 yr, the maximum thermal pulse has passed, the system has cooled substantially; the average dike temperature has dropped to $1/e$ of the initial average temperature and vigorous circulation has ceased (Fig. 4f). After 10 yr, the elevated temperatures have dropped and the system has returned to T values within 15% of initial background conditions.

In concert with the heat transport, the highest instantaneous fluid fluxes and fluid velocities (shown by velocity vectors) are recorded within the thermal plumes (Fig. 5a–f). Dike fracture is complete by ~ 0.4 yr, but the fracture permeability is lower than surrounding host sediments such that only minor fluid flow occurs within the intrusion. Time-integrated fluid flux reaches a maximum value, $520 m_{fluid}^3 / m_{rock}^2$, along the lateral extent of the dike in this short-lived system. Because the most rapid heating occurs within the pulses of upwelling fluid during initial plume formation, maximum heating rates migrate to coincide with each new unstable pulse of upwelling fluid. Heating rates remain high for only a short time, i.e., months, so that reaction overstepping is rapid and migrates in concert with the thermal plumes.

Mass transport of silica by diffusion, advection, dispersion, and reaction, is computed in the system as a function of time. Because silica concentration in the $SiO_2 - H_2O$ system reaches a maximum for this P near $380^\circ C$, concentrations in the fluid increase as the fluid warms. After reaching the maximum, silica then precipitates or reacts with continued heating. However, for this system temperatures in the host rocks typically remain below the concentration maxima except very near to the dike. Therefore, precipitation due to higher temperatures would not be expected.

For the isotropic, homogeneous κ system, silica is redistributed in the host rocks (Fig. 5a–f). Instantaneous silica concentrations in the fluid are higher in the focused upwellings of warm aqueous fluids due to increased solubility (Fig. 5a–f). In contrast, cool downwelling fluids contain lower concentrations of silica, leading to the development of silica plumes that mirror the upwelling and downwelling thermal plumes (cf. Figs. 4, 5). Silica movement becomes more diffuse and declines as fluid fluxes decrease with cooling (Fig. 5f). This results in broad zones of silica enrichment (relative to initial conditions) in the warmer upwelling zones and beneath the dike. The most significant increase in silica occurs at the lateral extension of the dike where the maximum fluxes of heat and fluid occur. Within the dike, the highest silica concentration tracks the temperature of the maximum silica solubility (and concentration) and migrates to the dike core with time (red zone, Fig. 5a–f). This temperature is below the fracture temperature,

therefore the higher silica concentrations occur after dike fracture. Concomitantly, silica concentrations increase slightly in the contact aureole, as it is advected from the upper margin of the dike.

After 10 yr, the time-integrated average of these temporally and spatially varying conditions results in permeability changes to the host rocks as silica transport and local reaction cause quartz to be dissolved, precipitated, or reacted (Fig. 6a). A complex interplay of temporally and spatially variable conditions defines the ultimate permeability distribution. The difference between the final and initial permeability (excluding the change in dike fracture permeability) throughout the system is relatively small; $\Delta \log K$ is within 0.005 in the aureole (Fig. 6a). For these initial conditions, permeability increases occur adjacent to the dike, above and below the intrusion, and along the dike's lateral extent, where warm fluids are focused. As the convection cells develop, quartz is dissolved in upwelling plumes, resulting in slight permeability increases in two broad fingers above the dike. As the silica-rich fluids cool, quartz is precipitated as it descends in the cooler, downward fingers of focused flow, or reacted, and a decrease in κ results (Fig. 6a). Precipitation also decreases permeability in a broad zone at the top of the domain and at the lower basal extent of the dike, where warmer fluids encounter cooler fluids. Decreasing κ would tend to refocus flow into the higher permeability zones, thus mitigating the permeability differences over time. This negative feedback will tend to defocus the flow over time and provides a mechanism which encourages the upwelling plumes to migrate laterally. Maximum differences in porosity due to dissolution are on the order of a few percent. Within the dike, permeability changes are primarily due to fracture. However, redistribution of silica also occurs in model calculations. Areas at the upper margin of the dike decrease in silica contents, thus increasing permeability, whereas at the lower margin of the dike, silica is precipitated or reacted and permeability is slightly decreased. Minor change is observed in κ at the lateral extent of the dike.

Maximum temperature attained at any time throughout the aureole created by this flow regime produces the isotherms shown in Figure 7a. Isotherms in the thermal aureole mirror the circulation cells and record the highly focused flow pattern as they pinch and swell above the dike. If kinetics are sufficiently rapid to mineralogically and isotopically respond to the thermal impact (i.e., isotherms \approx isograds), this thermal field would result in alteration zones of variable thickness above the intrusion. A very thin zone of elevated temperature is recorded laterally at the end of the dike due to the strongly focused fluid upwelling of the thermal boundary layer at the lateral edge of the intrusion. Beneath the intrusion, the contact aureole is much thinner and roughly constant in thickness. This type of fingering may, in part, explain the very small aureole with respect to the heat source, if the core is drilled through a narrow zone of elevated temperature (Fig. 7a). This system also produces large lateral heterogeneities in the thermal structure, despite the initial homogeneous permeability field.

Three-dimensional calculations for this system demonstrate that the upwelling plumes begin as rolls (narrow plumes in 2D) on the margins of the dike, and progress inward with time (Fig. 8a,b). These rolls become progressively unstable and separate into 3D fingers of warmer temperatures (Fig. 8c,d). Continued

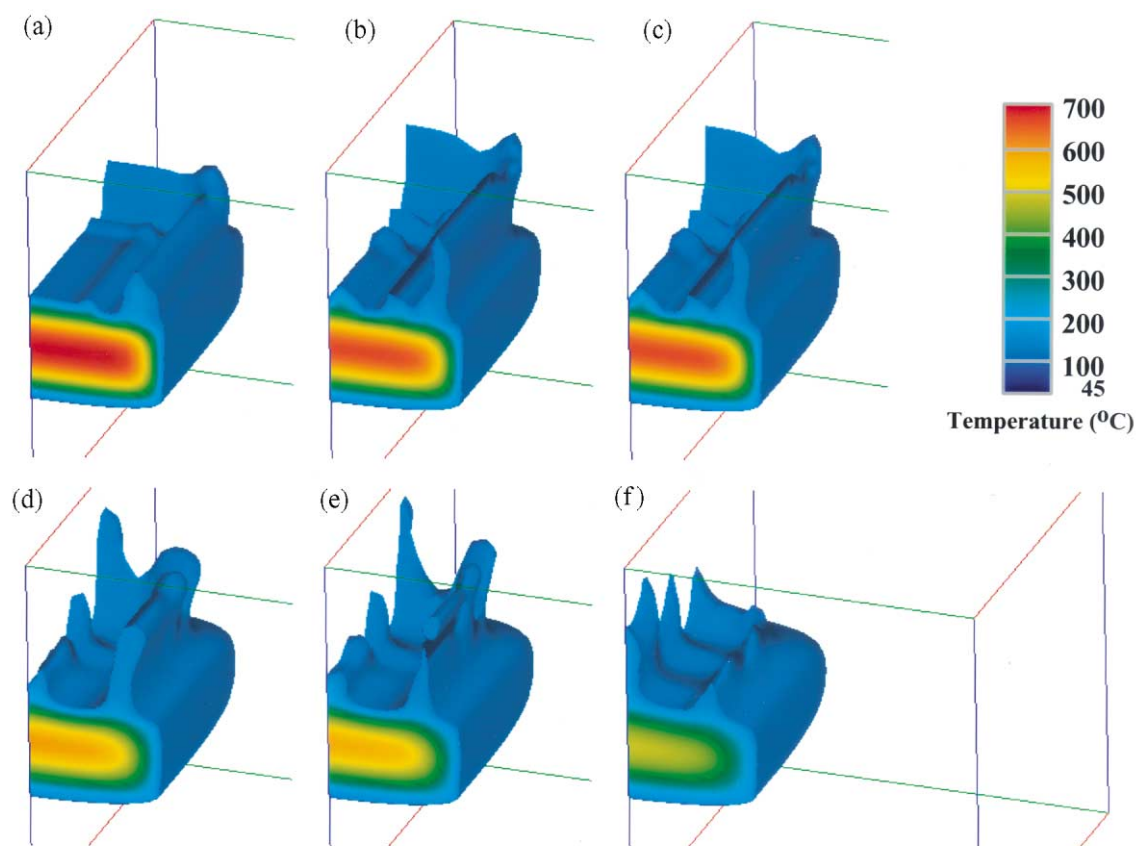


Fig. 8. Evolution of the thermal field for the homogeneous κ , 3D calculations as a function of time. Blue isosurface is for 155°C with colors indicating T values within the dike. (a) 0.05 yr, (b) 0.08 yr, (c) 0.1 yr, (d) 0.14 yr, (e) 0.15 yr, and (f) 0.24 yr.

evolution produces additional plumes with large vertical extent in the aureole (Fig. 8e,f). As in 2D calculations, these rolls are restricted to areas above the dike, separate into fingers, continue their upward movement, migrate laterally, and coalesce with time.

4.2. Anisotropic Permeability

In many regions, compaction of sediments results in preferred orientation of mineral grains reducing the ability of fluids to flow vertically. Decreasing the vertical permeability an order of magnitude below the horizontal permeability creates a barrier to vertical flow and introduces heterogeneities into the system. These heterogeneities result in a distinctly different style of heat and mass transfer in the host rocks.

Relative to the homogeneous, isotropic system, intrusion of the dike causes temperatures to increase in the host rocks more uniformly. As the fluid above the intrusion warms on the boundary layer, a single plume begins to rise above the end of the dike (Fig. 9a,b). With time, this single focused plume extends vertically and migrates inward as a wave of heated fluids, creating two distinct circulation cells above the dike (Figs. 9c–f, 10). Beneath the dike, fluids flow horizontally. No thermal boundary layer appears at the lateral extent of the dike, a function of the lower κ_z . Heating rates are maximized on the

inward edge of the plume and follow its lateral migration. The lower vertical permeability stifles vertical flow and a single plume (for this half space) remains. This temperature evolution is driven by advection of hot fluids. Mass fluxes are initially greatest proximal to the lower and upper edges (Fig. 10a,b). As the system evolves, high fluid fluxes migrate laterally inward, driving the plume of elevated temperatures above the dike toward the dike's center (Fig. 10c–f). Fluxes remain elevated above the dike but dissipate below the dike. Silica is swept from the upper and outer intrusion boundary and elevated silica in the fluid coincides with the migrating thermal plume (Fig. 10a–d). Asymmetry develops in silica fluid concentrations. The left side of the thermal plume has rising warm temperatures with increased silica concentrations. On the right side of the plume, an influx of cooler fluids at the top of the dike contains lower silica concentrations. With time, the silica-rich plume diffuses and becomes more vertical (Fig. 10e,f). The maximum time-integrated fluid flux for these conditions is nearly $475 m_{fluid}^2 / m_{rock}^2$ and occurs directly over the dike at the lateral extent.

For this flow regime, time-integrated changes in silica reaction produce broad regions of permeability change that occur asymmetrically around the dike. Precipitation results in lower permeability at the upper and lower corners of the dike and in

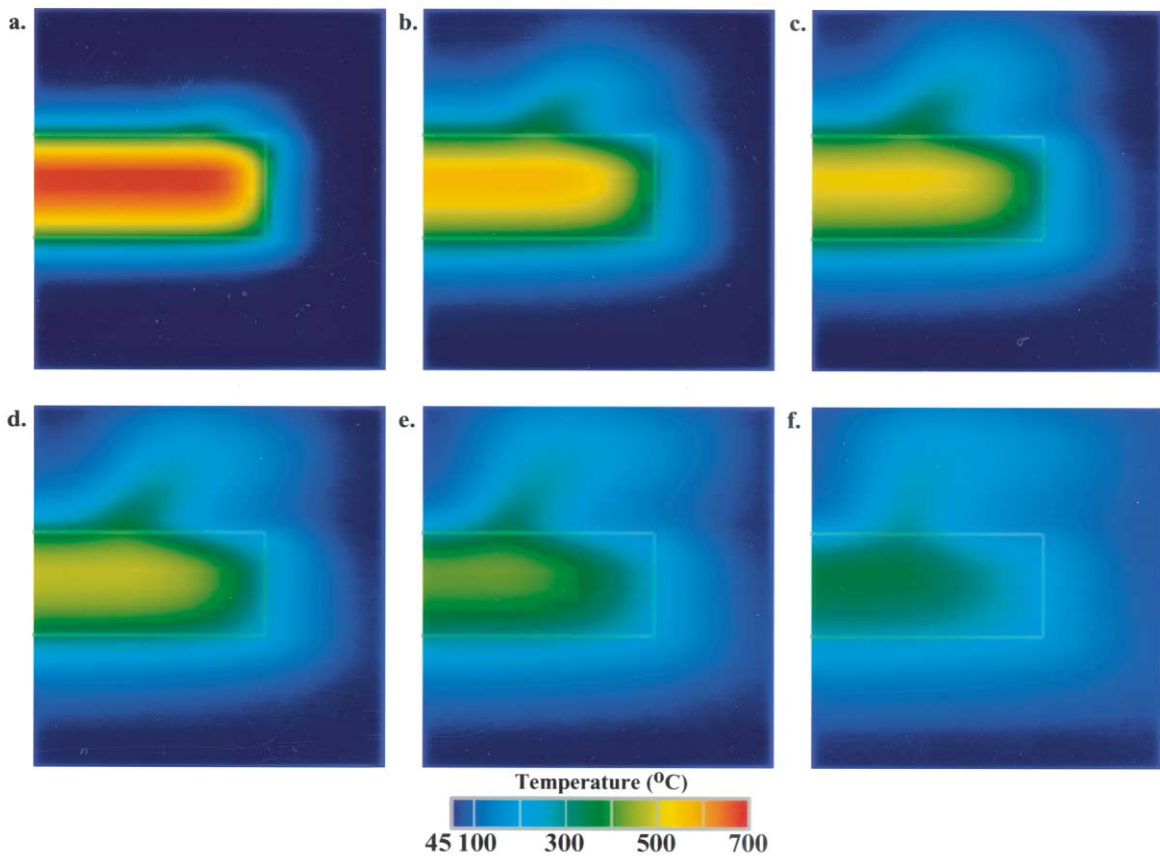


Fig. 9. Evolution of the thermal field for the anisotropic κ system as a function of time. (a) 0.1 yr, (b) 0.3 yr, (c) 0.4 yr, (d) 0.5 yr, (e) 0.7 yr, and (f) 1.0 yr. Gray box outlines the location of the dike.

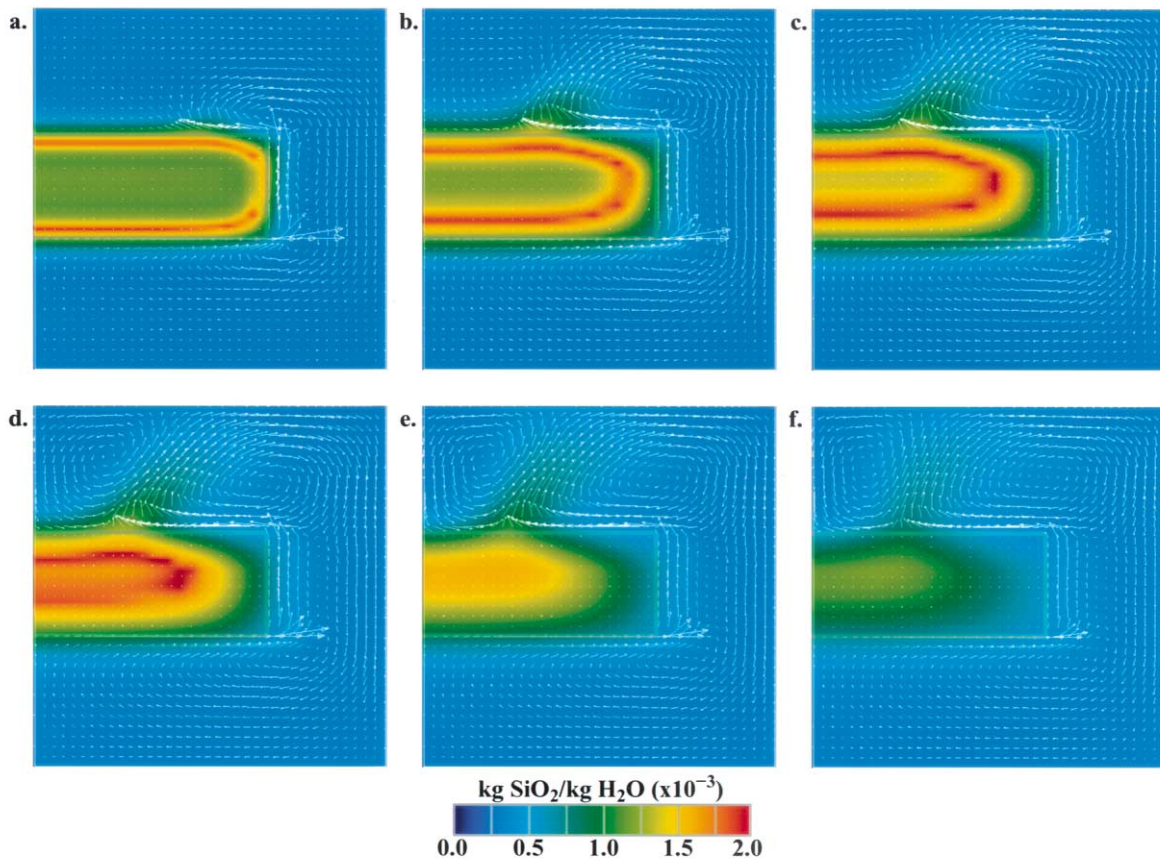


Fig. 10. (a-f) Transport of silica in the fluid for anisotropic κ as a function of time (given in Fig. 9) with velocity vectors that indicate the direction and magnitude of instantaneous flow. Gray box outlines the location of the dike.

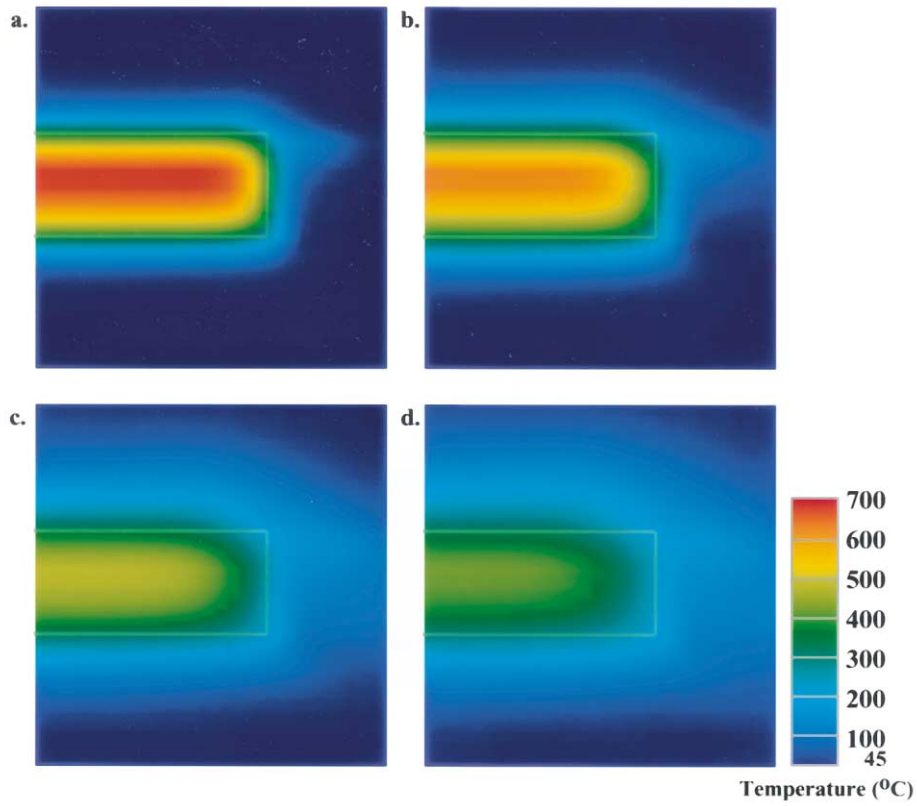


Fig. 11. Evolution of the thermal field for a layered κ distribution as a function of time. (a) 0.2 yr, (b) 0.4 yr, (c) 0.5 yr, (d) 1.0 yr. Gray box outlines the location of the dike.

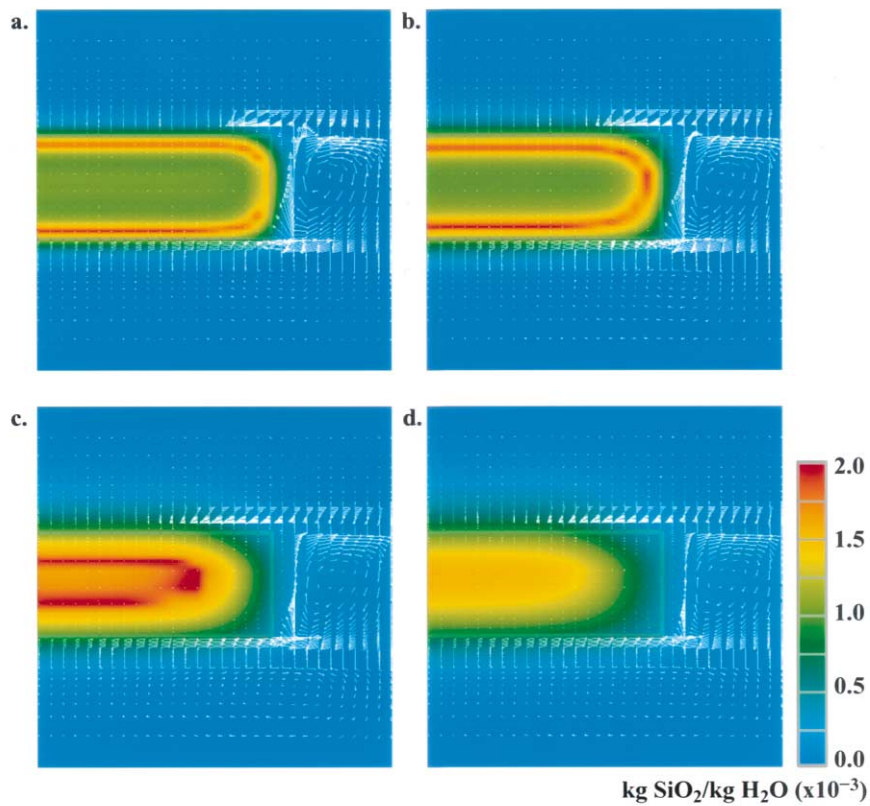


Fig. 12. (a–d) Transport of silica in the fluid for layered κ distribution as a function of time (given in Fig. 11) with velocity vectors that indicate the direction and magnitude of instantaneous flow. Gray box outlines the location of the dike.

a broad area centered over the dike (Fig. 6b). Within the dike, dissolution occurs and κ increases at the upper corner within a central zone. In contrast, quartz is precipitated or silica reacted within the lower corner of the dike.

The maximum temperature isotherms created by the anisotropic flow system are relatively smooth, varying from thin to thick to thinner, with a large region of elevated temperature centered above the dike due to the migration of the single plume (Fig. 7b). Below the dike isotherms are restricted, have a small vertical extent, and are uniform in thickness. Isotherms are compressed near the upper top of the dike where the circulation cells bring in cool fluids. A comparatively larger, asymmetric aureole develops around the intrusion, above, below, and laterally (cf. Fig. 7a–c).

4.3. Layered Permeability, Isotropic within Layer

Layered permeability also restricts vertical movement of heat and mass, and concentrates flow and transport within the more permeable units. Consequently, fluid fluxes, silica transport, and permeability changes are highest in these layers. The dike intrudes a more permeable zone dominated by siltstone and capped by the less permeable carbonate mudstone layers (Fig. 3). Heat is transferred from the dike more uniformly into the surrounding sediments, creating a broad diffuse zone of elevated temperatures above and below the dike (Fig. 11), in contrast to the focused upwelling zones observed in previous models (Figs. 4, 9). Heat transport initiates flow in the more permeable siltstone layer and a single, small plume develops and extends laterally off the upper corner of the dike immediately after intrusion (Figs. 11a,b, 12a,b). As fluids beneath the dike warm, flow begins and fluids move around the impermeable intrusion to escape upward where they drive the weak circulation cell at the lateral extent of the dike (Figs. 11c, 12c). Fluid flow also occurs in the overlying permeable zone, initially above the dike's lateral contact. The limited vertical extent of this zone allows only a small convection cell to develop (Figs. 11, 12). Flow continues in the permeable regions until the thermal driving force subsides at ~ 5 yr; mass flux decreases and a diffusive regime returns. The maximum time-integrated fluxes are smaller than those of previous calculations, $280m^3_{fluid}/m^2_{rock}$, and a greater amount of heat is transported by conduction. The highest flux occurs in the circulation cell off the end of the dike and around the bottom corner of the dike.

Silica transport is minor and occurs from the dike into the surrounding sediments in a broad diffuse aureole (Fig. 12a–d). Fluid flow is minor through the less permeable caprock. In the host rocks, silica is dissolved and κ increases below the dike where heated fluids flow around the dike and upward along the lateral extent. Minor dissolution occurs in the siltstones above the dike (Fig. 12a). Silica precipitation or reaction occurs in a small zone at the lower base of the dike and in the permeable units where the circulation cell develops. Precipitation occurs primarily away from the dike where circulation causes a cooling of fluids. To a lesser extent, κ decreases in the permeable layer above the dike. Precipitation or reaction occurs in the initially high permeability zones due to their more porous nature (Fig. 3) which promotes fluid flow, cooling, and precipitation or reaction of silica. Permeability changes are largest adjacent to the dike, both above and below, where the fluids on

the boundary are heated. Within the dike, precipitation occurs at the base and in a large region at the top of the dike (Fig. 7c).

Calculations for a layered permeability system result in the production of a broad thermal aureole surrounding the dike (Fig. 7c). High temperatures vary smoothly around the dike and have a larger horizontal extent at the dike's end (cf. Fig. 7a–b).

5. DISCUSSION AND CONCLUSIONS

Calculations of heat transport from the dike into the surrounding country rock suggest that host rocks remained at elevated temperatures for only a short time and that the metamorphic pulse was short-lived. Within ~ 10 yr, the excess thermal energy from dike emplacement dissipated and the system returned to near background conditions. Nucleation and growth of new minerals and isotopic exchange must have progressed over this relatively short time interval when reaction forces were of sufficient magnitude for transformations to occur.

Metamorphism was driven by advection of energy and by fluids that were out-of-equilibrium with the local environment. Advective transport of chemical components from the dike into the surrounding sediments probably created large chemical affinities that acted in concert with the thermal energy transport to drive mineralogical alteration of the original siltstones and mudstones. Advection also supplied nutrients for growth of the metamorphic minerals that record, in part, metasomatic constituents derived from the dike such as alkalis, alkaline earths, and fluorine. The exact amount of reaction overstepping due to infiltration of compositionally distinct fluids is difficult to access [e.g. Reaction Affinity $A_r = RT \ln (K/Q_r)$; Norton, 1987; Helgeson, 1987], in part because of the paucity of thermodynamic data for pectolite and apophyllite. However, due to the difference between initial and final mineral assemblages, chemical overstepping must have been substantial.

Addition of dissolved constituents (e.g., using silica) to the flow system alters fluid density and permeability and, consequently, impacts the transport of heat and fluid. For a homogeneous, isotropic permeability system without SiO_2 transport, a total of eight plumes develop for this half space, double the number of those formed in the identical system with SiO_2 transport. Higher temperatures and T_{max} contours extend to larger vertical distances above and below the dike (Fig. 7d, cf. 7a). This indicates that silica dampens the vigorous plume formation and vertical heat transport. Although the effective permeability change and subsequent feedback is minor due to SiO_2 dissolution, precipitation, or reaction, SiO_2 transport does significantly influence the resulting shape of the isotherms and the temperatures attained in the host rocks, primarily through fluid density changes that affect convection dynamics. In this case, convection is driven by chemical as well as thermal buoyancy.

These calculations demonstrate that large lateral heterogeneities in the thermal field were likely to have occurred in the contact aureole, even for homogeneous, isotropic systems. Initial heterogeneities in permeability are not a prerequisite for the development of a complicated flow and transport pattern (Fig. 8; cf. Gerdes et al., 1995; Marchildon and Dipple, 1998). As such, isotherms may not form uniform structures with boundaries characterized by exponentially increasing distance from

Table 3. Maximum temperatures ($^{\circ}\text{C}$) attained in the contact aureole with time of T_{max} in ().

Case: Mineral zone	Homogeneous κ		Anisotropic κ		Layered κ	
	center	end	center	end	center	end
Recrystallized calcite	166 (0.48)	202 (0.27)	307 (0.48)	240 (0.26)	307 (0.48)	240 (0.26)
Diopside	148 (0.51)	211 (0.28)	332 (0.43)	263 (0.19)	332 (0.41)	263 (0.15)
Pectolite (above)	207 (0.06)	250 (0.05)	359 (0.36)	303 (0.13)	307 (0.53)	289 (0.32)
Garnet	322 (0.06)	330 (0.05)	385 (0.36)	360 (0.13)	388 (0.53)	359 (0.32)
Dike						
Pectolite (below)	311 (0.15)	288 (0.10)	318 (0.19)	303 (0.15)	319 (0.18)	303 (0.15)
Diopside	224 (0.26)	194 (0.27)	245 (0.34)	226 (0.34)	246 (0.34)	226 (0.34)
Recrystallized calcite	163 (0.68)	147 (0.85)	189 (0.51)	175 (0.56)	204 (0.68)	192 (0.71)

the heat source, as has been demonstrated for convective systems (Parmentier and Schedl, 1981). A complex isotherm geometry is due to formation of upwelling and downwelling plumes, lateral translation of plumes, and SiO_2 dissolution/precipitation/reaction control on fluid flux. This leads to heterogeneity and variability in the isotherm signature that does not necessarily reflect the inherent heterogeneity of initial material properties. In fact, the calculation with the homogeneous permeability field has the most heterogeneous T_{max} and isotherm pattern. For example, comparison of temperature-time series for two positions at the same vertical distance above the intrusion, representative of the pectolite zone, but horizontally separated (one centered over the intrusion, 10 m from the dike's end, another point 5 m from the end) produces differences in T_{max} of 43°C for homogeneous κ , 56°C for anisotropic κ , and 18°C for the layered κ system (Table 3; Figs. 7, 13) demonstrating the lateral heterogeneities of the thermal field in T_{max} . The magnitude of this variation is more pronounced near the end of the dike. Large-scale layered heterogeneities in the permeability structure tend to dampen small-scale variations such that over time a more laterally uniform thermal aureole results, in contrast to stochastic κ structures which tend toward channeling to accentuate differences (Gerdes et al. 1995; Marchildon and Dipple, 1998; Aharonov and Spiegelman, 1997).

As a consequence of processes interacting with each other and the feedback inherent in the system, each of these calculations results in a spatially distinct contact aureole in T_{max} surrounding the dike. In all cases the contact aureole is asymmetric above and below the dike, similar to the rock record. The most spatially extensive aureole is developed above the dike for the layered system (Fig. 7c). The anisotropic κ system develops the widest aureole above the dike, but the aureole thins on either side; the thinning most pronounced near the end of the dike. For this case, if a vertical core were taken near the end of the dike, host rocks would record temperatures that warm, cool, then warm again. The homogeneous case results in very thin zones centered over the dike but which pinch and swell laterally; the 200°C zone has the smallest spatial extent. If kinetics are sufficiently rapid such that chemical alteration records peak temperatures attained in the thermal aureole, the aureole will preserve these complex high-temperature flow patterns. If not, these mineralogical zones represent advective isograds and reaction fronts, only generally related to isotherms (Marchildon and Dipple, 1998; Dutrow et al., 1999).

The data that motivated this work are from a single bore hole, so extensive interpretation of the 3D structure in the Blackened Smackover is difficult. However, we can place bounds on calculations and constrain the scenarios that were likely operative. Maximum temperatures can be compared for the different calculations at points representative of the pectolite, diopside, and recrystallized calcite zones (Table 3). With the exception of the homogeneous κ case, temperatures were highest at positions centered over the intrusion. However, maximum temperatures attained in the various calculations varied by nearly 150°C (Table 3). For the pectolite zone, $T_{max} = 250^{\circ}\text{C}$, 359°C , or 307°C for the homogeneous, anisotropic, and layered systems, respectively. The time at which T_{max} was reached also varied; 0.06, 0.36, 0.53 yr, respectively, but in all cases high T was a transient feature that was attained very early in the thermal history (Fig. 13). Rocks were heated for less than 1 yr. For the diopside zone, $T_{max} = 148^{\circ}\text{C}$, 332°C , or 332°C , for respective calculations and was attained at 0.51, 0.43, and 0.41 yr, respectively (Table 3). Depending on distance from the intrusive contact and the κ structure, the amount of time that the rocks remained at elevated temperatures ($\geq 200^{\circ}\text{C}$) also varies as shown by the temperature-time series at the pectolite zone for the three computational systems. Note the lateral heterogeneities in the temperatures recorded at the same vertical distance from the dike. Heating and cooling rates are distinctly different for each system (Fig. 13). For the homogeneous κ system, a sharp thermal spike is recorded at both horizontal locations above the intrusion (Fig. 13). Temperatures fall below 200°C in less than 0.25 yr. The centered circulation cell developed in the anisotropic κ system causes temperatures to remain elevated for longer periods, ~ 2 yr, whereas T dropped quickly at the end of the intrusion where cool fluids downwell. The layered κ system produces T that remained elevated for the longest time period, ~ 2.5 yr at the center, ~ 2 yr at the end, also suggesting that cooling histories were distinctly different.

If T_{max} isotherms are representative of mineralogical zones (i.e. isograds), the contact aureoles resulting from the anisotropic κ and the homogeneous κ calculations correspond more closely to the observed aureole and to the isograd widths recorded in the rocks and compare favorably with other P,T estimates. Previous calculations which include latent heat terms and higher intrusion temperatures produce aureoles approximately double in width, and are unlike zones recorded in the cores (Dutrow et al., 1997). Using an initial intrusion temperature of 875°C produces temperatures of 441, 389, 282°C for

Temperature Evolution - Pectolite Zone

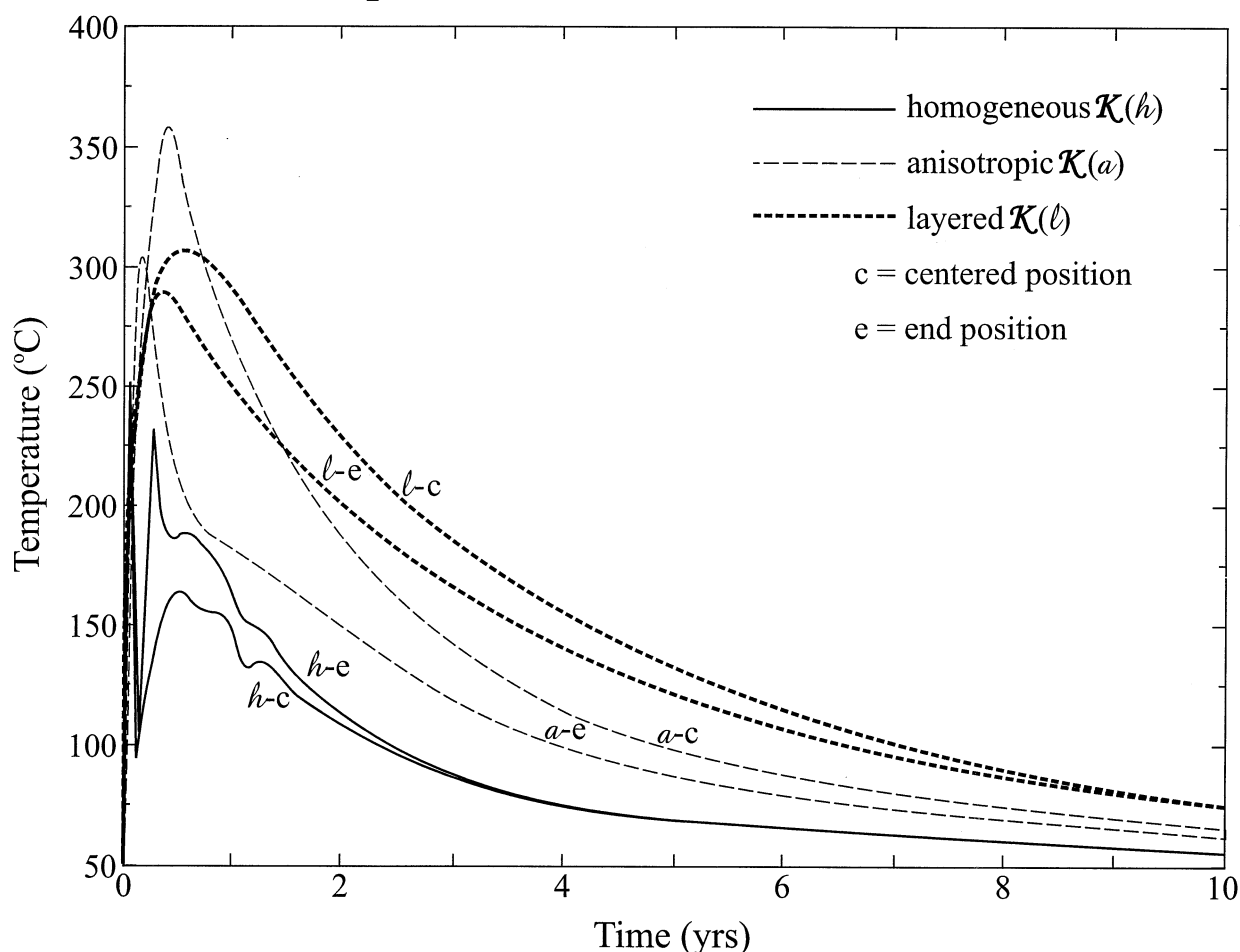


Fig. 13. Temperature–time series for positions above the dike equivalent to the distance of the pectolite zone (1.5 m) at horizontally separated locations (c = centered over the dike at 10 m from end, e = 5 m from the end of the dike).

the pct, diop, cal zones (the difference in temperatures at the contact is about half of the difference between initial and intrusion temperatures).

These restricted zones of elevated temperatures also indicate that the thermal influence of the dike is of limited spatial extent. The window of gas production is between about 150–300°C (Blatt, 1992). Examining Figure 7 suggests that temperatures reached these conditions in a relatively small area. Therefore, gas generation from an intrusion of this size would be areally limited as would the convection cell generated by the intrusion. Either multiple dikes of the size described here or larger igneous intrusions at depth would be required to produce the heat necessary to generate the gas contained in this area.

The heating rate and rapid movement of the thermal pulse suggest that significant chemical alteration occurred in less than 3 yr, in response to infiltration of chemically out-of-equilibrium fluids that resulted in large chemical affinities. Transport of silica, alkalis, and F from the dike into the surrounding sediments may explain the observed mineralogical changes in the host rock and the dike. The model calculations also suggest that silica was redistributed from the upper portion of the dike and

transported into the surrounding sediments. Redistribution of silica from the top margin of the dike into the surrounding sediments could, in part, supply the silica necessary for formation of the apophyllite and pectolite. This may also explain the lack of a chilled top dike margin (all calculations suggest dissolution) in contrast to the preservation of a chilled margin at the lower contact (where calculations show precipitation/reaction). Quartz is absent in the matrix near the dike. Although the dike is silica undersaturated, advection can overcome local diffusional forces to transport silica into the host rocks. Results of these calculations provide constraints on temperatures attained in the host rocks in the absence of precise geothermometric assemblages and demonstrate the limited extent of the thermal zone for gas generation. They also demonstrate that complicated flow patterns are generated in systems with isotropic permeability structures and by feedback within the system.

Acknowledgments—Original inspiration for many aspects of this study was provided by Prof. Helgeson, beginning with a most memorable field trip to metasomatized rocks of the Aegean region. There flowing

fluids were intimately intermingled with rocks and theory to advance our understanding of fluid–rock interactions. What a remarkable adventure—thank you and may there be more. Samples for the petrographic study were made available by Ezat Heydari, formerly of the Basin Research Institute at LSU. Dr. Heydari is thanked for bringing the problem to our attention and for many helpful discussions on the Smackover formation. This research was supported by the Institute of Geophysics and Planetary Physics (IGPP) through a grant to BLD and BJT administered by the Regents of the University of California and the Los Alamos National Laboratory (LANL). CWG was partially supported by the IGPP and Earth and Environmental Sciences Division at LANL. BLD also acknowledges support for the computational aspects of this study from NSF-EAR9814418 and thanks N. Rosenberg for early collaboration. Greg Dipple, Ron Frost, Ray Joesten, and John Schumacher are thanked for providing critical, useful, and insightful reviews which greatly improved the manuscript.

Associate editor: B. R. Frost

REFERENCES

- Aharonov E. and Spiegelman M. (1997) Three-dimensional flow and reaction in porous media: Implications for Earth's mantle and sedimentary basins. *J. Geophys. Res.* **102**, 14, 821–14,833.
- Anovitz L. M. and Essene E. J. (1987) Phase equilibria in the system $\text{CaCO}_3\text{-MgCO}_3\text{-FeCO}_3$. *J. Petr.* **28**, 389–414.
- Bear J. (1972) *Dynamics of Fluids in Porous Media*. Elsevier, New York. 73–82.
- Berman R. C. (1988) Internally-consistent thermodynamic data for minerals in the system $\text{Na}_2\text{O-K}_2\text{O-CaO-MgO-FeO-Fe}_2\text{O}_3\text{-Al}_2\text{O}_3\text{-SiO}_2\text{-TiO}_2\text{-H}_2\text{O-CO}_2$. *J. Petrol.* **29**, 445–522.
- Berman R. C. (1991) Thermobarometry using multi-equilibrium calculations: A new technique, with petrological applications. *Can. Mineral.* **29**, 833–855.
- Blatt H. (1992) *Sedimentary Petrology*. W. H. Freeman, New York. 431–432.
- Bolton E. W., Lasaga A. C., and Rye D. M. (1999) Long-term flow/chemistry feedback in a porous medium with heterogeneous permeability: Kinetic control of dissolution and precipitation. *Am. J. Sci.* **299**, 1–68.
- Bowers T. S., Jackson K. J., and Helgeson H. C. (1984) *Equilibrium Activity Diagrams for Coexisting Minerals and Aqueous Solutions at Pressures and Temperatures to 5 kb and 600°C*. Springer-Verlag, New York. 106–109.
- Byerly G. (1991) Igneous activity. In *The Geology of North America, The Gulf of Mexico Basin*. (ed. A. Salvador). Geol. Soc. Am. J. Boulder, pp. 91–108.
- Canals M. and Meunier J. D. (1995) A model for porosity reduction in quartzite reservoirs by quartz cementation. *Geochim. Cosmochim. Acta* **59**, 699–709.
- Carmichael I. S. E., Turner, F. J., and Verhoogen, J. (1974) *Igneous Petrology*, McGraw-Hill, New York, 508–514.
- Carrera J., Heredia J., Vomvoris S., and Hufschmied P. (1990) Modeling of flow on a small fractured monzonitic gneiss block. In *Hydrogeology of Low Permeability Environments* (eds. S. P. Neuman and I. Neretnieks). International Association of Hydrogeologists, Hydrogeology: Selected Papers **2**, 115–167. Heise, Hannover.
- Cherkaoui A. S. M. and Wilcock W. S. D. (1997) Thermal fluxes associated with the 1993 diking event on the Coaxial segment, Juan de Fuca Ridge: A model for the convective cooling of a dike. *J. Geophys. Res.* **102**, 24887–24902.
- Christensen C. (1997) Effects of heat transport and fluid flow during contact metamorphism in the Carter Hope-Fee Well, Northeastern Louisiana. Unpublished master's thesis, LSU, Baton Rouge, LA 1–77.
- Cook S. J., Bowman J. R., and Forster C. B. (1997) Contact metamorphism surrounding the Alta Stock: Finite-element model simulation of heat- and $^{18}\text{O}/^{16}\text{O}$ mass transport during prograde metamorphism. *Am. J. Sci.* **297**, 1–55.
- Clarke S. P., Jr. (Ed.) (1966) *Handbook of Physical Constants*. Geol. Soc. Am., Memoir 97. p. 23,563.
- Dutrow B. L., Henry D. J., Christensen C., Gable C. W., Travis B. J., and Heydari E. (1997) Blackened Smackover: Thermal evolution and mass transfer adjacent to a subsurface alkalic igneous dike in Northern, Louisiana. *Gulf Coast Assoc. Geol. Soc. Trans.* **47**, 131–139.
- Dutrow B. L., Foster C. T., Jr., and Henry D. J. (1999) Tourmaline-rich pseudomorphs in sillimanite zone metapelites: Demarcation of an infiltration front. *Am. Mineral.* **84**, 794–805.
- Dutrow B., Foster C. T., Jr., Gable C. W., and Travis B. J. (2000a) 4D thermal models for regional-contact metamorphism in NW Maine. *Abs. Prog. Geol. Soc. Am. Meeting* **32**, A113.
- Dutrow B., Gable C. W., Travis B. J., and Foster C. T., Jr. (2000b) Effects of fluid flow, permeability and pluton fracturing on T-t paths in metamorphic aureoles: Implications for models of nucleation and mineral growth. *EOS, Am. Geophys. Union* **81**, F1379–1380.
- Echols J. B., Zimmerman R. K., and Goddard D. A. (1994) An integrated geochemical and geological approach for determining hydrocarbon generation-migration patterns: Central Gulf Coast Basin. *Gulf Coast Assoc. Geol. Soc. Trans.* **44**, 193–203.
- Elder J. W. (1967) Steady free convection in a porous medium heated from below. *J. Fluid Mech.* **27**, 29–48.
- Fehn U. and Cathles L. M. (1979) Hydrothermal convection at slow-spreading mid-ocean ridges. *Tectonophysics*. **55**, 239–260.
- Fehn U., Green K. E., Von Herzen R. P., and Cathles L. M. (1983) Numerical models for the hydrothermal field at the Galapagos Spreading Center. *J. Geophys. Res.* **88**, 1033–1048.
- Fontaine F. J., Rabinowicz M., and Boulegue J. (2001) Permeability changes due to mineral diagenesis in fractured crust: Implications for hydrothermal circulation at mid-ocean ridges. *Earth Planet. Sci. Lett.* **184**, 407–425.
- Garven G., Ge S., Person M., and Sverjensky D. (1993) Genesis of stratabound ore deposits in the midcontinent basins of North America. I. The role of regional groundwater flow. *Am. J. Sci.* **293**, 497–568.
- Gerdes M. L., Baumgartner L. P., and Person M. (1995) Stochastic permeability models of fluid flow during contact metamorphism. *Geology* **23**, 945–948.
- Glikson M., Mastalerz M., Golding S. D., and McConachie B. A. (2000) Metallogenesis and hydrocarbon generation in northern Mount Isa Basin, Australia: Implications for ore grade mineralization. In *Organic Matter and Mineralisation* (eds. M. Glikson and M. Mastalerz), pp. 149–184. Kluwer Academic Publishers, Dordrecht.
- Hanson R. B. (1995) The hydrodynamics of contact metamorphism. *Geol. Soc. Am. Bull.* **107**, 595–611.
- Helgeson H. C. (1968) Evaluation of irreversible reactions in geochemical processes involving minerals and aqueous solutions: I. Thermodynamic relations. *Geochim. Cosmochim. Acta* **32**, 853–877.
- Helgeson H. C. (1987) Application of some moderation theorems to metasomatic processes. In *NATO Advanced Study Institute on Chemical Transport in Metasomatic Processes* (ed. H. C. Helgeson), pp. 189–238. Reidel, Amsterdam.
- Helgeson H. C. (1992) Effects of complex formation in flowing fluids on the hydrothermal solubilities of minerals as a function of fluid pressure and temperature in the critical and supercritical regions of the system H_2O . *Geochim. Cosmochim. Acta* **56**, 3191–3207.
- Helgeson H. C., Delany J. M., Nesbitt W. J., and Bird D. K. (1978) Summary and critique of the thermodynamic properties of rock-forming minerals. *Am. J. Sci.* **278A**, 1–229.
- Heydari E., Byerly G. R., and Henry D. J. (1997) Contact metamorphism and over maturation of organic matter associated with an igneous intrusion in the Smackover Formation, Northeastern Louisiana. *Gulf Coast Assoc. Geol. Soc. Trans.* **47**, 201–213.
- Johnson J. W. and Norton D. (1991) Critical phenomena in hydrothermal systems: State, thermodynamic, electrostatic, and transport properties of H_2O in the critical region. *Am. J. Sci.* **291**, 541–648.
- Johnson J. W., Oelkers E. H., and Helgeson H. C. (1992) SUPCRT92-A software package for calculating the standard molal thermodynamic properties of minerals, gases, aqueous species and reactions from 1 bar to 5000 bar and 0 to 1000°C. *Comput. Geosci.* **18**, 899–947.
- Kidwell A. L. (1949) Mesozoic igneous activity in the northern Gulf Coastal Plain. Ph.D. thesis, Univ. Chicago.
- Kidwell A. L. (1951) Mesozoic igneous activity in the northern Gulf Coastal Plain. *Gulf Coast Assoc. Geol. Soc. Trans.* **1**, 182–199.
- Lapwood E. R. (1948) Convection of a fluid in a porous medium. *Proc. Cambridge Phil. Soc.* **44**, 508–521.

- Lichtner P. C., Steefel C. I., and Oelkers E. H. (eds.) (1996) *Reactive Transport in Porous Media*. Reviews in Mineralogy **34**, 438 pp. Min. Soc. Am., Washington, DC.
- Lowell R. P. (1991) Modeling continental and submarine hydrothermal systems. *Rev. Geophys.* **29**, 457–476.
- Lowell R. P., Van Capellen P., and Germanovich L. N. (1993) Silica precipitation in fractures and the evolution of permeability in hydrothermal upflow zones. *Science* **260**, 192–194.
- Ludvigsen A., Palm E., and McKibbin R. (1992) Convective momentum and mass transport in porous sloping layers. *J. Geophys. Res.* **97**, 12,315–12,325.
- Lyons P. L. (1957) Geology and geophysics of the Gulf of Mexico. *Gulf Coast Assoc. Geol. Soc. Trans.* **7**, 1–10.
- Manning C. E. (1997) Coupled reaction and flow in subduction zones: Silica metasomatism in the mantle wedge. In *Fluid Flow and Transport in Rocks* (eds. B. Jamtveit and B. W. D. Yardley), pp. 139–148. Chapman & Hall.
- Manning C. E. and Bird D. K. (1990) Fluorian garnets from the host rocks of the Skaergaard intrusion: Implications for metamorphic fluid composition. *Am. Mineral.* **75**, 859–873.
- Marchildon N. and Dipple G. (1998) Irregular isograds, reaction instabilities, and the evolution of permeability during metamorphism. *Geology* **26**, 15–18.
- Moldovanyi E. P. and Walter L. M. (1992) Regional trends in water chemistry, Smackover formation, southwest Arkansas: Geochemical and physical controls. *AAPG Bull.* **46**, 864–894.
- Moody C. L. (1949) Mesozoic igneous rocks of the northern Gulf Coastal Plain. *AAPG Bull.* **33**, 1410–1428.
- Navrotsky A. (1981) Thermodynamics of mixing in silicate glasses and melts. In *Thermodynamics of Minerals and Melts* (eds. R. C. Newton, A. Navrotsky, and B. J. Wood), pp. 189–205. Springer-Verlag, New York.
- Norton D. (1977) Fluid circulation in the Earth's crust. In *The Earth's Crust*, Geophys. Monograph **20**, 693–704. Am. Geophys. Union, Washington, DC.
- Norton D. (1979) Transport phenomena in hydrothermal systems. The redistribution of chemical components around cooling magmas. *Bull. Mineral.* **102**, 471–486.
- Norton D. (1987) Advective metasomatism. In *NATO Advanced Study Institute on Chemical Transport in Metasomatic Processes* (ed. H. C. Helgeson), pp. 123–132. Reidel, Amsterdam.
- Norton D. and Taylor H. P., Jr. (1979) Quantitative simulation of the hydrothermal systems of crystallizing magmas on the basis of transport theory and oxygen isotope data: An analysis of the Skaergaard Intrusion. *J. Petrol.* **20**, 421–486.
- Oelkers E. and Helgeson H. C. (1988) Calculation of the thermodynamic and transport properties of aqueous species at high-pressures and temperatures: Aqueous tracer diffusion coefficients of ions to 1000°C and 5 KB. *Geochim. Cosmochim. Acta* **52**, 63–85.
- Ohmoto H. and Kerrick D. (1977) Devolatilization equilibria in graphitic systems. *Am. J. Sci.* **277**, 1013–1044.
- Parmentier E. M. and Schedl A. (1981) Thermal aureoles of igneous intrusions; some possible indications of hydrothermal convective cooling. *J. Geol.* **89**, 1–22.
- Rabinowicz M., Boulege J., and Genton P. (1998) Two- and three-dimensional modeling of hydrothermal convection in the sedimented Middle Valley segment, Juan de Fuca Ridge. *J. Geophys. Res.* **103**, 24045–24065.
- Raymond A. C. and Murchison D. G. (1988) Development of organic maturation in thermal aureoles of sills and its relation to sediment compaction. *FUEL* **67**, 1599–1608.
- Rosenberg N. D. and Spera F. J. (1990) Role of anisotropic and/or layered permeability in hydrothermal systems. *Geophys. Res. Lett.* **17**, 235–238.
- Roux J. and Hamilton D. (1976) Primary igneous analcite; an experimental study. *J. Petrol.* **17**, 244–257.
- Sassen R. and Moore C. H. (1988) Framework of hydrocarbon generation and destruction in eastern Smackover Trend. *AAPG Bull.* **72**, 649–663.
- Snow D. T. (1965) A parallel plate model of fractured permeable media. Ph.D. thesis, University of Calif., Berkeley, CA.
- Spear F. S. (1993) Metamorphic Phase Equilibria and Pressure-Temperature-Time Paths. Monograph, Min. Soc. Am., Washington, D.C. p. 653.
- Travis B. J., Janecky D. R., and Rosenberg N. D. (1991) Three-dimensional simulations of hydrothermal circulation at mid-ocean ridges. *Geophys. Res. Lett.* **18**, 1441–1444.
- U.S. National Committee for Rock Mechanics (1996) *Rock Fractures and Fluid Flow: Contemporary Understanding and Applications*. National Academy Press, Washington, DC.
- Walther J. and Helgeson H. C. (1977) Calculation of the thermodynamic properties of aqueous silica and the solubility of quartz and its polymorphs at high temperatures and pressures. *Am. J. Sci.* **277**, 1315–1351.
- Wells J. T. and Ghorso M. S. (1991) Coupled fluid flow and reaction in mid-ocean ridge hydrothermal systems: The behavior of silica. *Geochim. Cosmochim. Acta* **55**, 2467–2481.
- Wilcock W. S. D. (1998) Cellular convection models of mid-ocean ridge hydrothermal circulation and the temperature of black smoker fluids. *J. Geophys. Res.* **103**, 2585–2596.
- Wood J. R. and Hewett T. A. (1982) Fluid convection and mass transfer in porous sandstones—a theoretical model. *Geochim. Cosmochim. Acta* **46**, 1707–1713.
- Zimmerman R. K. and Sassen R. (1993) Hydrocarbon transfer pathways from Smackover source rocks to younger reservoir traps in the Monroe Gas Field, Northeast Louisiana. *Gulf Coast Assoc. Geol. Soc. Trans.* **43**, 473–480.

APPENDIX

Background

Various studies have considered the modeling of hydrothermal circulation in porous/fractured media, as far back as Lapwood (1948) and Elder (1967). Voluminous literature exists on this topic. Perhaps the most relevant body of literature for our study pertains to circulation near magmatic intrusions beginning with Norton (1977), Fehn and Cathles (1979), Norton and Taylor (1979), and Fehn et al. (1983). Rosenberg and Spera (1990) examined the role of layering and anisotropy in hydrothermal systems. Travis et al. (1991) presented the first full 3-D simulations of a mid-ocean ridge system, and simulated both the background, off-axis convection and the dynamic hydrothermal system evolution in response to a magmatic intrusion. Additional literature exists for modeling circulation in mid-ocean ridge environments (Lowell, 1991). Cherkaoui and Wilcock (1997) considered convective cooling of a dike, Wilcock (1998) related cellular convection to black smoker temperatures. Rabinowicz et al. (1998) discussed 2D and 3D modeling of hydrothermal convection in the sedimented Middle Valley segment of the Juan de Fuca ridge. Numerical hydrothermal convection in contact metamorphic aureoles has been investigated by, for example, Hanson (1995), Cook et al. (1997), Dutrow et al. (2000a,b).

Several studies considered chemical reaction in hydrothermal systems beginning with the work of Helgeson (1968) (see also Helgeson, 1992). More recently, for systems with silica, Wood and Hewett (1982) evaluated 1D porosity reduction by quartz in a thermal gradient, Wells and Ghorso (1991) used a 1D steady-state model to determine κ , and ϕ changes along a flow path as a function of silica precipitation and dissolution, and Manning (1997) used a 1D analytical solution for coupled flow and SiO_2 reaction in the mantle wedge with respect to the stable mineral assemblage in the $\text{MgO-SiO}_2\text{-H}_2\text{O}$ system (see also papers in Lichtner et al., 1996). Lowell et al. (1993) used analytical models for isolated and parallel fractures to evaluate fracture closure from SiO_2 precipitation in upflow zones based on constant values of concentration change as a function of T and P. Aharonov and Spiegelman (1997) used first-order linear kinetics for SiO_2 , constant fluid density, and a linear gradient in SiO_2 solubility to understand precipitation and dissolution driven by flux and pressure in a system without advective heat transport. Bolton et al. (1999) coupled flow, driven by temperature differences in boundaries, and SiO_2 reaction based on kinetics, in an isotropic κ system with linear fluid properties to determine regions of dissolution and precipitation around spherical grains. Fontaine et al. (2001) considered permeability changes due to hydrothermal circulation at mid-ocean ridges. The preceding discussion is by no means comprehensive on the topic of hydrothermal convection

in porous media. Instead, it is intended to demonstrate that this is an area of active research yet having a long history.

Equations

Equations governing the flow of fluids in porous media follow. Conservation of fluid mass is described by the anelastic form:

$$\nabla \cdot (\rho_f \tilde{v}) = 0 \quad (\text{A1})$$

where ρ_f is fluid density and \tilde{v} is Darcy fluid velocity, which neglects fast changes in density (sound waves) and which assumes no mass sources or sinks, but does allow for density variations in space $\rho_f(\mathbf{x}, P, T)$.

Fluid momentum transport is expressed by Darcy's law, which is valid when inertial effects are negligible, at sufficiently slow fluid flow rates (i.e., valid for Reynolds number ≤ 1 ; Bear, 1972).

$$\tilde{v} = -\frac{\kappa}{\mu} (\nabla P + \rho_f g \hat{z}) \quad (\text{A2})$$

The intrinsic permeability tensor, κ , can vary spatially and temporally. Dynamic viscosity, μ in (Pa s), is a function of T and P, and g is the gravitational constant, 9.8 ms^{-2} (Table 2).

The conservation of energy equation assumes that the fluid and matrix are in local thermal equilibrium. The equation follows the form used in Travis et al. (1991);

$$\frac{\partial}{\partial t} \left[(1 - \phi) \rho_s c_{ps} T + \phi \rho_f I_f + (1 - \phi) \rho_s \sqrt{\frac{\beta}{\pi}} Q_c \cdot \int_{T_{(t)}}^{T_{(t_0)}} e^{-\beta(T - T_{solid})^2} dT \right] + \nabla \cdot (\tilde{v} \rho_f E_f) = \nabla \cdot (K_e \nabla T) \quad (\text{A3})$$

where subscript s, is for properties of the solid, subscript f, is for properties of the fluid, and c_p is heat capacity of the porous media ($J \text{ kg}^{-1} \text{ } ^\circ\text{C}^{-1}$). The first term on the left-hand side above represents change in energy content of the rock, where ϕ is flow porosity. Total porosity is the sum of isolated porosity, which does not contribute to the flow, and the flow porosity; $\phi_{iso} + \phi_{flow} = \phi_{total}$. For these calculations, isolated porosity is assumed to be negligible such that $\phi_{total} = \phi_{flow}$. The second term in Eqn. A3 represents fluid energy; the third term is latent heat release, where Q_c is the latent heat of crystallization ($J \text{ kg}^{-1}$), which is released in a continuous manner around the crystallization temperature, T_{solid} ; the fourth term is advection of fluid enthalpy; and the right-hand side term is diffusion of thermal energy. The narrowness of the temperature interval around T_{solid} during which crystallization occurs is controlled by β . Large values of β correspond to narrow intervals of crystallization in T. The internal energy, I_f , and the enthalpy, E_f functions (of P,T) are from Johnson and Norton (1991).

The thermal conductivity, K_e represents a phase-volume-weighted sum of the thermal conductivities of each phase (i.e., fluid and rock):

$$K_e = \phi K_f + (1 - \phi) K_s \quad (\text{A4})$$

For small values of ϕ , K_e is approximately equal to K_s . Silica transport is controlled by

$$\frac{\partial}{\partial t} (\phi \rho_f C_f) + \nabla \cdot \tilde{v} \rho_f C_f = \frac{1}{Le_o} \nabla \cdot \left(\frac{D}{D_o} \nabla \rho_f C_f \right) - k_r \phi \rho_f (C_f - C_{sol,lim}) \quad (\text{A5})$$

where the transport mechanisms include advection, diffusion, and precipitation/dissolution. C_f is the concentration in the fluid. Le_o is the Lewis number (thermal diffusivity/chemical diffusivity at reference conditions). The solute diffusivity, D , is a function of temperature (after Oelkers and Helgeson, 1988). Dissolution and precipitation of SiO_2 is determined from the temperature- and pressure-dependent surfaces for solubility, $C_{sol,lim}$, of quartz (SUPCRT92; Johnson et al., 1992; Helgeson et al, 1978). k_r is the reaction rate.

Permeability is assumed to exist through a fracture network, with the parallel plate flow model (Snow, 1965) applying locally in each frac-

ture. However, rather than explicitly modeling flow through individual fractures we used the widely adopted convention (Carrera et al, 1990; U.S. National Committee for Rock Mechanics, 1996) of computing an equivalent permeability. The equivalent permeability is a combination of the porous media and fracture permeability, using a porous medium, Darcy-law approach. This assumes that the same fracture number density applies within each computational cell. Also, all fractures within a computational cell are of the same aperture, and the fracture number density in a cell does not change over time. The initial values of effective permeability and flow porosity in a cell determine the number density and aperture of fractures in that unit. In our calculations, the initial effective permeability is constant within a geologic unit but may change between units. Fracture aperture evolves over time due to precipitation and dissolution. The fracture number density, along with cell size, determine the number of fractures in each computational cell. The relationships between flow porosity, effective permeability, number of fractures, and fracture aperture can be derived from the definition of flow porosity as fracture volume divided by total cell volume:

$$\phi = Nw \left(\frac{A_{xy}}{A_{xy} \Delta z} \right) = N^* \frac{w}{\Delta z} \quad (\text{A6})$$

where w is fracture aperture. N is the number of fractures in a computational cell of width Δz , A_{xy} is the fracture face area, and Δz is the length of the cell in the direction perpendicular to the fracture face; and from the definition of mass flux through a computational cell side:

$$\begin{aligned} q_x &= - \left(\frac{w^2}{12} * w \Delta y * N \right) \frac{\Delta P}{\mu \Delta x} = - \left(\frac{w^3}{12} * N * \frac{\Delta y}{A_{yz}} \right) * \frac{\Delta P}{\mu \Delta x} * A_{yz} \\ &= - \left(\frac{w^3}{12} * \frac{N}{\Delta z} \right) \frac{\Delta P}{\mu \Delta x} * A_{yz} = - \left(w^2 \frac{\phi}{12} \right) * \frac{\Delta P}{\mu \Delta x} * A_{yz} \end{aligned} \quad (\text{A7})$$

In Eqn. A7, the fluid flux, q_x , in direction x (the argument is identical for the other coordinate directions) is written in the numerically convenient finite difference form in which velocity is multiplied by the total cell side area, A_{yz} , perpendicular to the direction of flow rather than the actual open area. After substituting from Eqn. A6, the effective permeability is shown to have the form

$$\kappa_e = \frac{w^2 \phi}{12} \quad (\text{A8})$$

From Eqn. A8, the initial w can be found if κ and ϕ are known (Snow, 1965). N is then obtained from Eqn. A6. Subsequently, as SiO_2 dissolves or precipitates or reacts, fracture width changes. The change in solid-phase SiO_2 due to dissolution, precipitation, or reaction is assumed to occur uniformly on the fracture faces in a computational cell. It follows from Eqn. A6 that the ratio of new to old porosity is equal to the new to old fracture width ratio, while Eqns. A8 and A6 together show that the ratio of new to old permeability values is equal to the cube of the ratio of new to old fracture widths, in keeping with the cubic flow law assumption.

The rate of change of fracture aperture due to precipitation/dissolution is computed from

$$\frac{dw}{dt} = k_r (C_{sol,lim} - C_f) \frac{\rho_f \phi \Delta \Omega}{\rho_{\text{SiO}_2} A_{xy}} = k_r (C_{sol,lim} - C_f) \frac{N \rho_f w}{\rho_{\text{SiO}_2}} \quad (\text{A9})$$

where k_r is the reaction rate and $C_{sol,lim}$ is the temperature- and pressure-dependent solubility limit.

Numerical solution of the mathematical model proceeds as follows. The spatial domain is discretized into a set of nonoverlapping computational cells that exactly cover the domain. In each computational cell, initial values of pressure, temperature, density, and concentrations are specified. The solution is advanced in time through a series of discrete time steps; each time step size is determined from the velocity component magnitudes and the size of the diffusion/dispersion terms. The dependent variables are updated at each time step through an iterative process. First, Eqn. A2 is substituted into Eqn. A1, providing an equation that is solved for pressure at the next time value, using previous time step values for densities and temperatures. Fluid velocity components are then computed for each cell, using the new pressure

and the previous time step (old) values of all other dependent variables. The time step size is computed, followed by the transport of heat and transport of solutes. The new temperature and density fields are determined from the equation-of-state using the new pressure and energy content fields. Finally, the fracture width field is updated (a function of

precipitation and dissolution) from Eqn. A9, followed by porosity and permeability updates. The iterative process is repeated at each time step. Iterations are continued until T and P fields on successive iterations vary by less than a prescribed tolerance, typically on the order of 10^{-7} , providing a very good mass and energy balance.